

Article

The Mineral Chemistry of Magnetite and Its Constraints on Ore-Forming Mechanism in the Sandaozhuang Skarn-Type W-Mo Deposit in East Qinling, China

Zhijie Zeng ¹, Uzair Siddique ¹, Miaojun Sun ², Qin Gao ¹, Yanting Chen ¹, Lei Chen ^{3,*} and Zilong Li ^{1,*}¹ Ocean College, Zhejiang University, Zhoushan 316000, China; zengzhijie@mail.zju.edu.cn (Z.Z.)² Engineering Exploration and Survey Department, Power China Huadong Engineering Corporation Limited, Hangzhou 311122, China³ Ministry of Natural Resources Key Laboratory of Metallogeny and Mineral Assessment, Institute of Mineral Resources, Chinese Academy of Geological Sciences, Beijing 100037, China

* Correspondence: chenlei@126.com (L.C.); zilongli@zju.edu.cn (Z.L.)

Abstract: The Sandaozhuang super-large W-Mo deposit is located in the southern margin of the North China Craton, within the well-known East Qinling Mo mineralization belt, and is one of the typical skarn-type W-Mo deposits in China. Based on EMPA and LA-ICP-MS analyses, major and trace elements were presented, and the mineral chemistry of magnetite at various mineralization stages was discussed. Combining field observations, petrography, and geochemical characteristics, the magnetite at the Sandaozhuang deposit can be classified into three types, namely early-magmatic-stage high-temperature magnetite (Mag1), potassic-alteration-stage magnetite (Mag2), and retrograde-alteration-stage magnetite (Mag3). The Mag1 and Mag2 magnetites primarily occurred in granites in association with potassium (K) feldspar and biotite, whereas Mag3 is associated with metallic sulfide minerals that occurred mainly in vein-like structures in skarn. The three magnetites Mag1, Mag2, and Mag3 can be distinguished as having magmatic, magmatic–hydrothermal transition, and hydrothermal origins, respectively. All three types of magnetite exhibit a depletion of high-field-strength elements (HFSEs) such as Zr, Hf, Nb, Ta, and Ti, and large-ion lithophile elements (LILEs) including Rb, K, Ba, and Sr, compared to the mean continental crust composition. Conversely, they are enriched in elements such as Sn, Mo, V, Cr, Zn, and Ga. Mag3 showed no significant depletion of Co, Ni, Cu, and Bi, indicating that the influence of coexisting sulfides on the composition of magnetite at the Sandaozhuang deposit is limited. There are systematic variations in major and trace elements from Mag1 to Mag3, which exhibited similar patterns in trace element spider and rare earth element diagrams, and Y/Ho ratio, indicating a consistent source for the three types of magnetite. The changes in V and Cr contents and (Ti + V) vs. (Al + Mn) diagram of magnetite at the Sandaozhuang deposit reflected the evolution of ore-forming fluids with an initial increase in oxygen fugacity and a subsequent decrease, as well as a gradual decrease in temperature during skarn mineralization. The early high-temperature and high-oxygen-fugacity magmatic fluids became W and Mo enriched by hydrothermal fluid interaction. The rapid change in fluid properties during the retrograde alteration stage led to the precipitation of scheelite and molybdenite.

Keywords: magnetite; mineral chemistry; ore-forming mechanism; Sandaozhuang W-Mo deposit; East Qinling



Citation: Zeng, Z.; Siddique, U.; Sun, M.; Gao, Q.; Chen, Y.; Chen, L.; Li, Z. The Mineral Chemistry of Magnetite and Its Constraints on Ore-Forming Mechanism in the Sandaozhuang Skarn-Type W-Mo Deposit in East Qinling, China. *Minerals* **2023**, *13*, 1091. <https://doi.org/10.3390/min13081091>

Academic Editors: Daniel Marshall, Guoxue Song, Mingjian Cao, Wenyuan Liu and Chao Zhao

Received: 9 July 2023

Revised: 2 August 2023

Accepted: 11 August 2023

Published: 15 August 2023



Copyright: © 2023 by the authors. Licensee MDPI, Basel, Switzerland. This article is an open access article distributed under the terms and conditions of the Creative Commons Attribution (CC BY) license (<https://creativecommons.org/licenses/by/4.0/>).

1. Introduction

Magnetite is a ubiquitous accessory and crucial metallic mineral formed in various geological settings, including sedimentary, igneous, and hydrothermal environments. Its tetrahedral and octahedral sites can accommodate numerous trace elements, such as Al³⁺, Nb⁵⁺, Ta⁵⁺, Mo⁴⁺, W⁴⁺, Ti⁴⁺, Si⁴⁺, Ge⁴⁺, V³⁺/V⁴⁺, and others [1,2]. The concentration of these elements is intricately linked to the fluid and/or magma composition, oxygen fugacity

(fO_2), crystallographic factors, and element partitioning behavior [3–5]. Magnetite is a common constituent in a wide range of lithological units and has significant implications for the genesis of rocks and ore deposits. Its widespread occurrence in diverse petrogenetic and metallogenic systems provides a unique research window for exploring the formation mechanisms of granites and ore deposits, as well as an effective tool for ore deposit exploration and prospecting [6–13].

The Sandaozhuang super-large molybdenum (tungsten) deposit is a typical skarn-type deposit located at the eastern margin of the East Qinling molybdenum polymetallic metallogenic belt. It has a total molybdenum metal reserve of 672,500 tons (a mean grade of 0.115%) and associated tungsten metal reserve of 502,460 tons (a mean grade of 0.117%). It also contains 3.98 million tons of sulfur and 22 tons of rhenium [14]. Together with the adjacent Nannihu and Shangfanggou porphyry-type molybdenum deposits, the Sandaozhuang deposit constitutes the world-class Nannihu molybdenum polymetallic ore district. Previous studies on the deposit's geological features, mineralization age, ore-forming fluids, and geochemical characteristics of ore-forming rocks [14–16] indicated that the deposit's mineralization and alteration are comparable to those of typical skarn-type tungsten–molybdenum deposits worldwide [17]. However, the metallogenic mechanism of the Sandaozhuang deposit, particularly the changes in physicochemical conditions during the mineralization process, remains understudied.

The previous studies on the Sandaozhuang deposit examined the evolution of ore-forming fluids using garnet [18] and scheelite [16]. However, these studies were limited to specific stages of mineralization and did not investigate the fluids throughout the entire process from magmatism to mineralization. As a result, the role of fluid properties during the pre-mineralization stage in W-Mo mineralization has been overlooked. Magnetite is widely present throughout the entire mineralization stages of the Sandaozhuang deposit and provides important insights into the genetic mechanisms of the deposit based on the patterns of its geochemical composition changes. In this study, we selected different types of magnetite from different stages of the Sandaozhuang deposit as research objects, based on detailed field investigations and mineral identifications. Trace element analyses using an electronic microprobe analyzer and in situ LA-ICP-MS were performed, and the genesis of magnetite and constraints of the mineralization process from the perspective of fluid properties were discussed.

2. Regional Geology

The Qinling orogenic belt is divided into four tectonic units from the north to the south of the southern margin of the North China Craton, the North Qinling orogenic belt, the southern Qinling orogenic belt, and the northern margin of the Yangtze Craton [19]. The Qinling molybdenum metallogenic belt is mainly developed in the southern margin of the North China Craton and the North Qinling orogenic belt. The Sanbao and Shangdan faults mark the northern and southern boundaries, respectively, while the Sandaozhuang tungsten–molybdenum deposit is located in the Luanchuan mining district on the southern margin of the North China Craton (Figure 1).

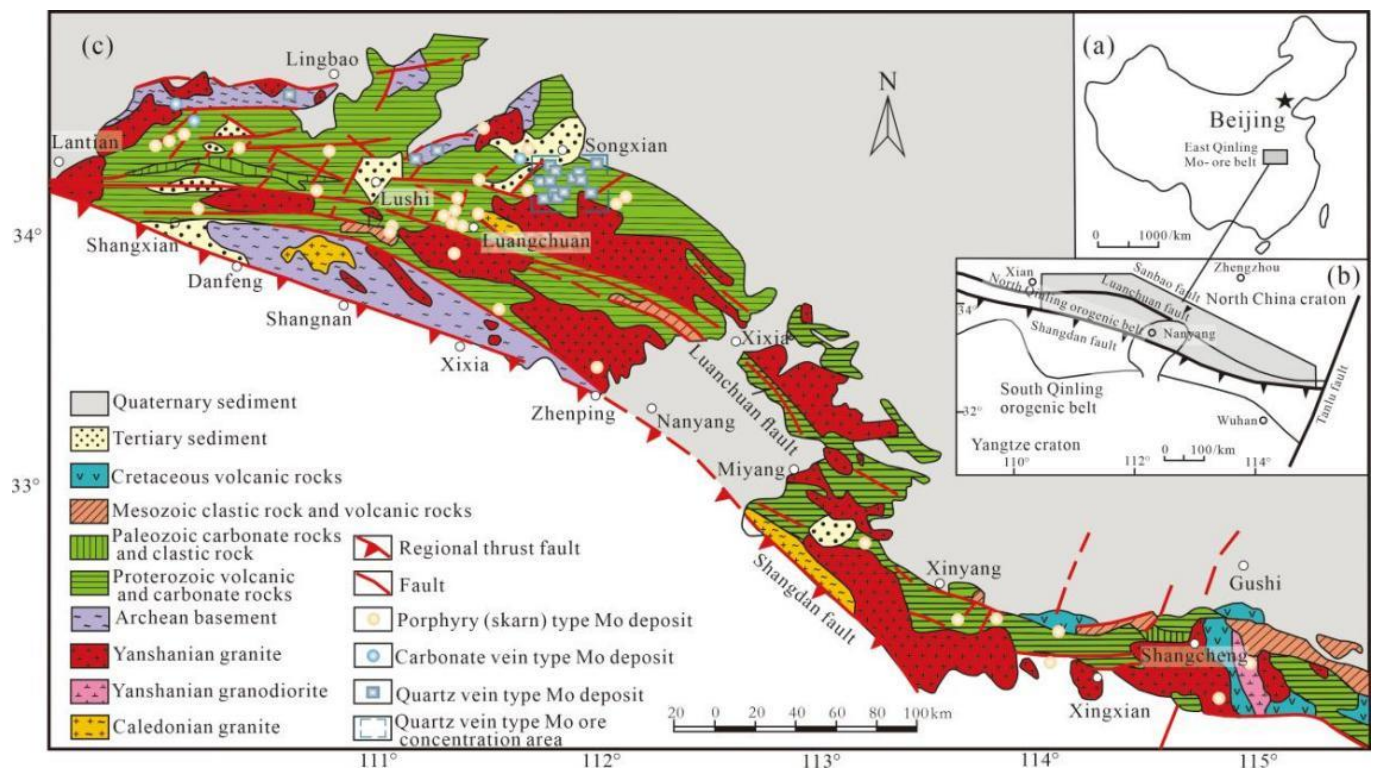


Figure 1. (a) Location of Qinling orogenic belt; (b) tectonic schematic map of Qinling orogenic belt; (c) geological map of molybdenum metallogenic belt in East Qinling Mountains (modified after [20]).

The regional stratigraphy in the study area is characterized by a double-layered crustal structure of a crystalline basement and sedimentary cover [21]. The crystalline basement mainly consists of the Neoproterozoic–Paleoproterozoic Taihua Group metamorphic rock series, while the cover includes the Middle Paleozoic Xionger Group volcanic rock series, the Middle–Neoproterozoic Guandaokou Group and Luanchuan Group terrestrial clastic rocks and carbonate rocks, and the Neoproterozoic–Lower Paleozoic Taowan Group shallow marine carbonate rocks [22] (Figure 1). The large-scale molybdenum, tungsten, lead, zinc, and gold mineralization in the eastern Qinling region is mainly related to the Mesozoic granites. The southern margin of the North China Craton, where the study area is located, is characterized by frequent magmatic activity and a wide distribution of various magmatic rocks, including volcanic rocks, gabbro, and quartz diorite (Figure 1). The complex multi-stage tectonic framework of the southern margin of the North China Craton is dominated by faults with NWW–SEE direction, overlaid by NE-trending and NNE-trending secondary fault zones. The Luanchuan fault, the most important fault in the Luanchuan mining district, underwent several brittle–ductile deformations during the Mesozoic orogeny. A series of NE-trending fault structures were superimposed on the Luanchuan fault, which is an intruded space for ore-bearing porphyry and its driven hydrothermal mineralization system, controlling the distribution of granitoids and molybdenum, tungsten, and other metal deposits in the region [23].

3. Ore Deposit Geology

The Sandaozhuang deposit, located in northwestern Luanchuan County, Henan Province, covers an area of 2.51 km² and is a part of the world-renowned Luanchuan molybdenum mining field, together with the adjacent Nannihu porphyry molybdenum deposit and Shangfanggou porphyry–skarn molybdenum–iron deposit. The mining area is dominated by the Neoproterozoic San Chuan Formation (Pt_{3s}) and Nannihu Formation (Pt_{3n}) of the Luanchuan Group, as the main ore-bearing formations in the area (Figure 2). In addition, lower orebodies have been discovered in the upper section of the Baishuzhuang

Formation at deeper levels in the Sandaozhuang mining area [24]. The Sanchuan Formation is mainly distributed in the Shibapan area in the northern part of the Sandaozhuang deposit, and in the Nanzhuang and Beizhuang regions situated in the eastern section of mining district, and consists of metasandstone and hornfels. The Nannihu Formation occurs in the upper Donggounao, Nannihu, Sandaozhuangling, Zushimiao, and Taibaoshan areas, and is mainly composed of hornfels and quartzite.

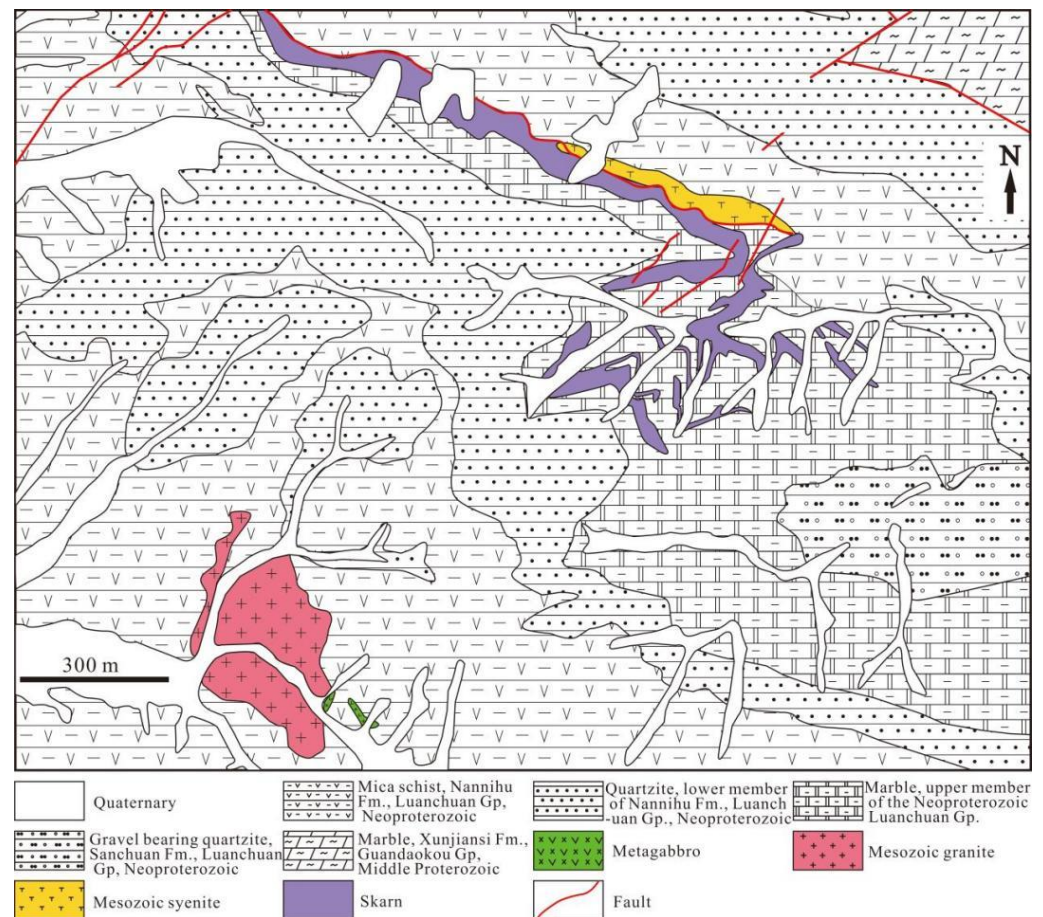


Figure 2. Geological map of Sandaozhuang mining area (modified after [14]).

The deposit is located in the northeastern inner and outer contact zone of the Nannihu granite porphyry, with molybdenum as the main ore and tungsten as the minor ore (Figure 3). The area of the Nannihu granitic porphyry is approximately 0.12 km², and the porphyry body is mainly distributed in the Nannihu mining area (Figures 2 and 3). A small amount of porphyry bodies exists in the deep part of the Sandaozhuang mining area and are rarely developed in the internal skarn. The main characteristics of the Sandaozhuang deposit are the hornfels alteration of the surrounding rock and the skarn in the outer contact zone, identified as a skarn-type deposit [15].

The mineralization process can be divided into six stages based on the characteristics of vein cross-cutting relationships and mineral assemblages of the magmatic stage (I), quartz-K-feldspar-biotite-magnetite stage (II), early silicate skarn stage (III), retrograde alteration stage (IV), quartz-sulfide stage (V), and quartz-carbonate stage (VI) (Figure 4). The main features of the six stages are as follows.

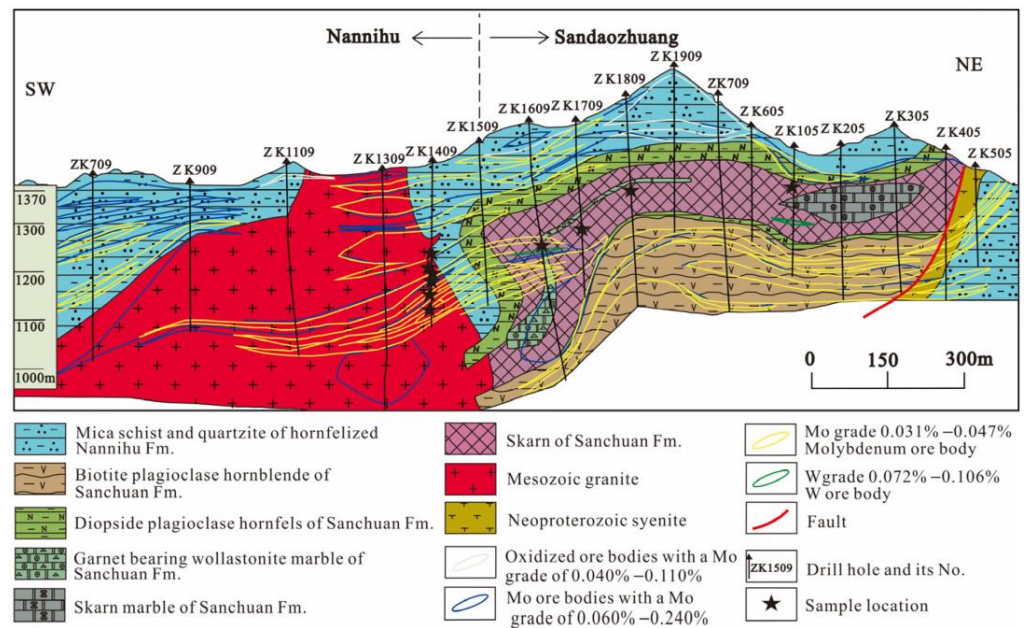


Figure 3. The geological section along the No. 9 exploration line of the Sandaozhuang–Nannihu deposit (modified after [25]).

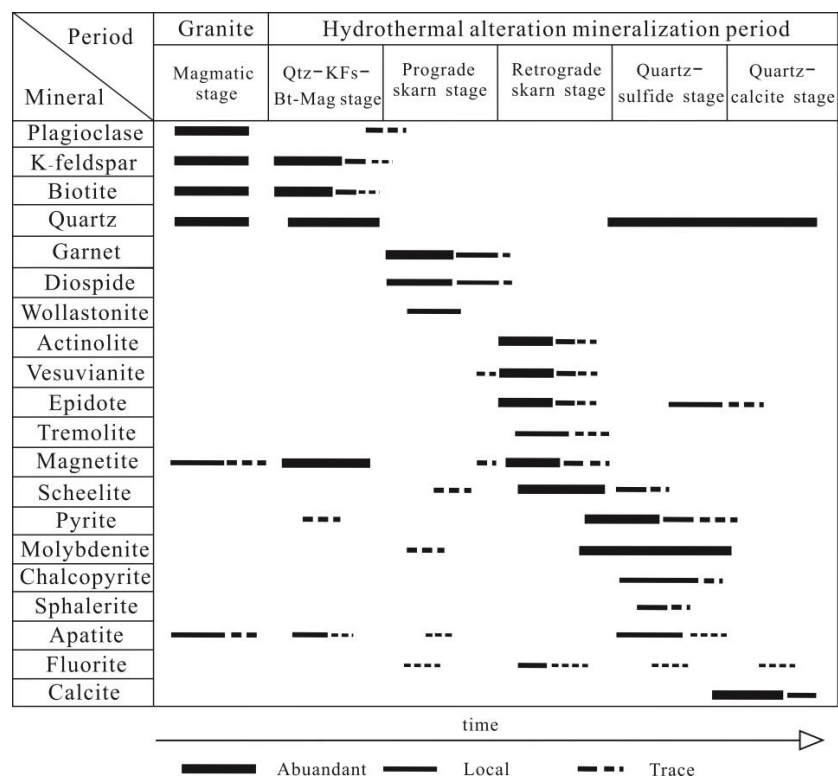


Figure 4. Mineral formation sequence of the Sandaozhuang W-Mo deposit.

- (1) The magmatic stage (I) is the stage of granitic porphyry formation associated with mineralization. During this stage, minerals such as biotite, plagioclase, K-feldspar, quartz, apatite, and magnetite are formed (Figure 5a,b and Figure 6a–c). Mag1 occurs as an accessory mineral in the granitic porphyry, and magnetite is commonly enclosed within biotite and K-feldspar phenocrysts, as a result of early magmatic crystallization, with a small grain size ranging from 0.1 to 0.2 mm, mostly in ovoid or ellipsoid shapes (Figure 6a–c).

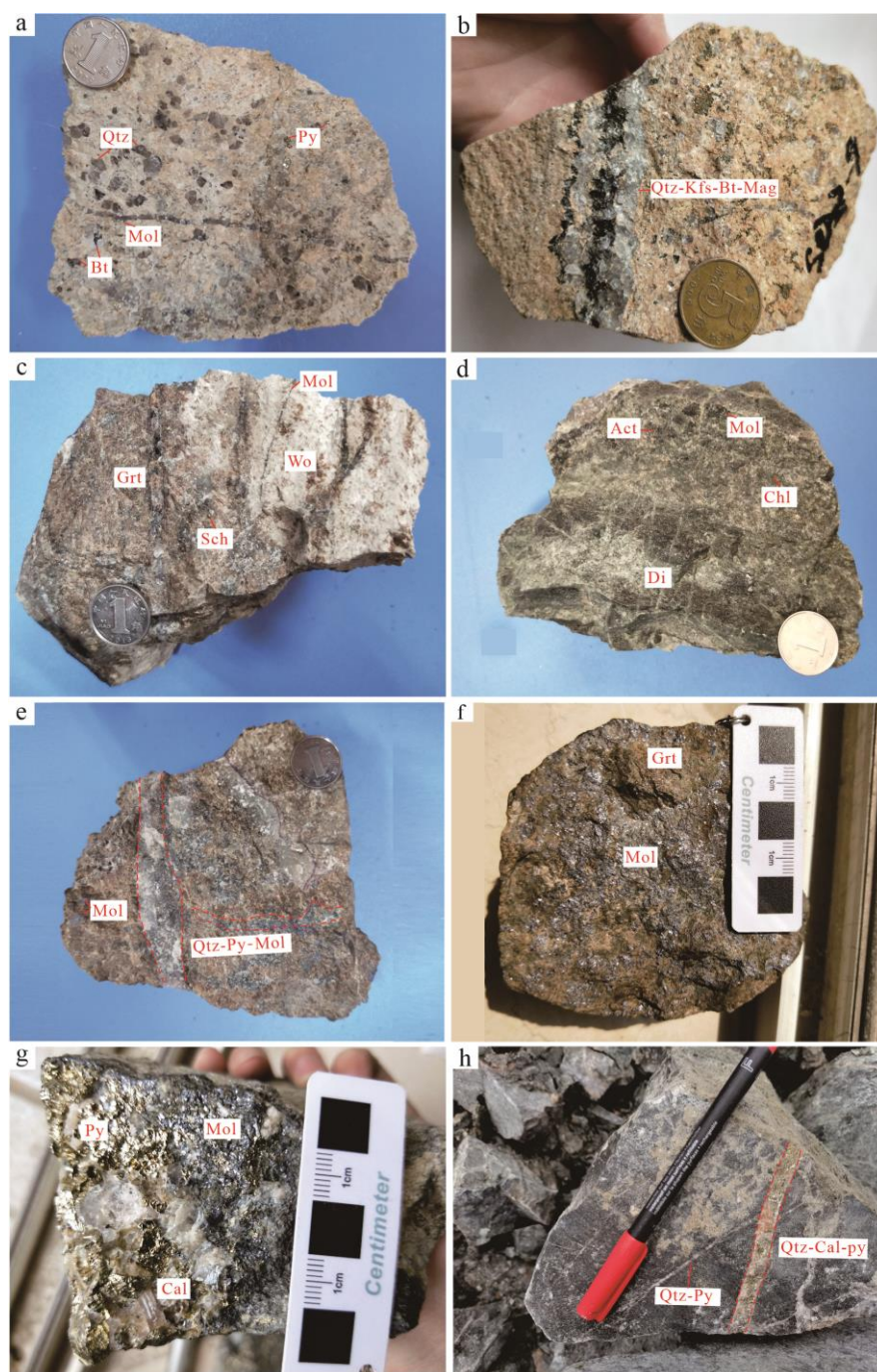


Figure 5. Photos of hand specimens of granite porphyry and skarn ore in the Sandaozhuang W-Mo deposit. (a) Granite porphyry, Mag1 coexisting with feldspar and quartz phenocrysts, and small veins of molybdenite interspersed within it; (b) quartz-K-feldspar-biotite-magnetite veins intercalated in the granite porphyry, Mag2 coexisting with K-feldspar and biotite; (c) garnet-wollastonite-silicate skarn ore, molybdenite is disseminated mineralization, scheelite is star shaped mineralization and coexists with Mag3; (d) actinolite-diopside-silicate skarn ore, coexistence of Mag3 and retrograded actinolite; (e,f) skarn ore, quartz-pyrite-molybdenite veins intercalated in garnet silicate skarn, with molybdenite mineralization in disseminated and vein forms; (g,h) hornfels ore, with quartz-pyrite, quartz-calcite-pyrite veins interspersed within it. Notes: Grt = garnet, Di = diopside, Wo = wollastonite, Qtz = quartz, Act = actinolite, Sch = scheelite, Mol = molybdenite, Chl = chlorite, Cal = calcite, Py = pyrite, Kfs = K-feldspar, Mag = magnetite, Bt = biotite.

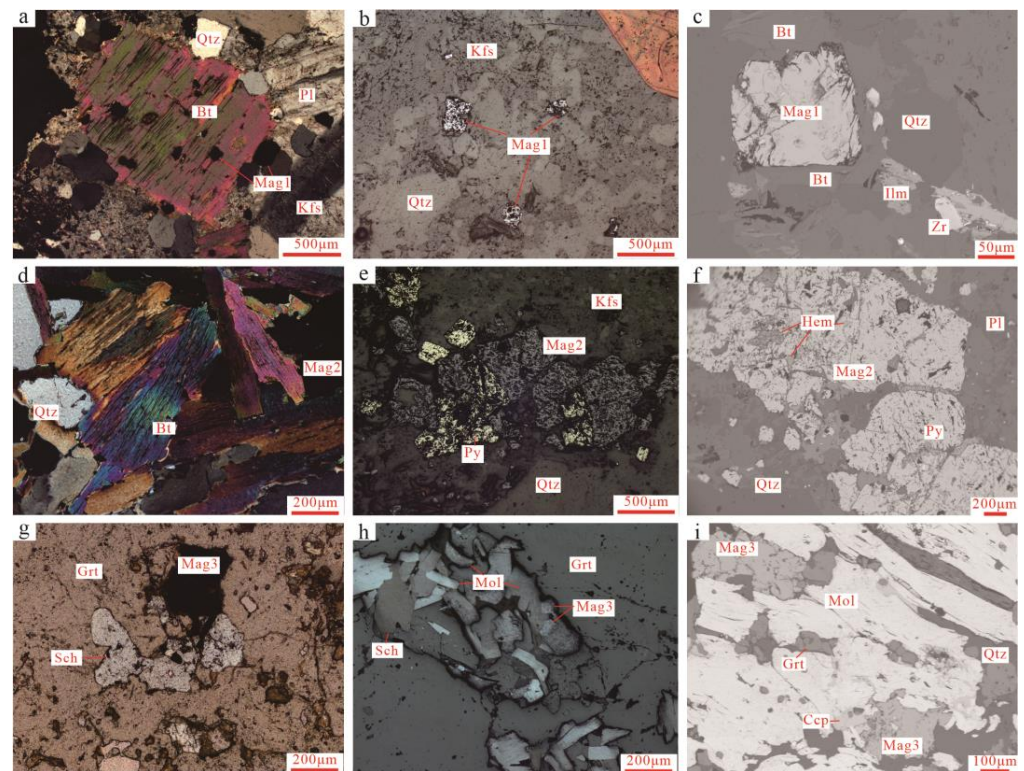


Figure 6. Photomicrographs of the mineral assemblage from Sandaozhuang W-Mo deposit. (a,b) Mag1 coexisting with biotite and plagioclase phenocrysts in the granite porphyry; (c) BSE image showing Mag1 coexisting with biotite, quartz, and ilmenite in the granite porphyry; (d,e) Mag2 closely coexists with pyrite, quartz, and K-feldspar in the quartz-K-feldspar vein; (f) BSE image showing Mag2 coexisting with pyrite and plagioclase in the quartz-K-feldspar vein; (g,h) Mag3 coexists with irregular scheelite and sheet and bundle molybdenite in the retrograde altered silicate skarn; (i) BSE image showing Mag3 coexisting with garnet and dendritic molybdenite. Note: Ccp = chalcopyrite, Zr = zircon, Pl = plagioclase, Ilm = ilmenite. The abbreviated names of other minerals are shown in Figure 5.

- (2) The stage (II) with quartz-K-feldspar-biotite-magnetite assemblage (potassic alteration stage) is characterized by the formation of minerals such as quartz, K-feldspar, biotite, magnetite, and pyrite. K-feldspar includes K-feldspar altered with a sheet-like or linear distribution, and K-feldspar associated with quartz and biotite (Figures 5b and 6d–f). Magnetite is common in this stage, usually appearing as aggregates, forming intergrowths with pyrite. A small amount of molybdenite occurred in thin veins or impregnations, appearing with K-feldspar alteration. Magnetite is commonly distributed on both sides of the veins, appearing in granular aggregates (Figure 5b).
- (3) The early silicate skarn stage (III) is mainly characterized by the formation of anhydrous silicate minerals, predominantly garnet and diopside (Figure 5c), as well as minor amounts of wollastonite and vesuvianite, and the formation of small amounts of scheelite.
- (4) The late silicate skarn stage (retrograde stage) (IV) is mainly characterized by the formation of a large number of hydrous silicate minerals, such as vesuvianite, chlorite, tremolite, epidote, zoisite, and minor amounts of quartz and apatite. At the same time, this stage also formed a large amount of scheelite and magnetite (Figure 5d–f), which is the main mineralization stage for scheelite. The scheelite occurs as subhedral to euhedral grains intermittently distributed in the interstices between garnet and diopside or intercalated in quartz veins in the skarn, often forming intergrowths, inclusions, or crosscutting relationships with molybdenite. It is distributed more in the middle part

- of the thin veins. Magnetite in the silicate skarn minerals commonly coexists with garnet, zoisite, and pyrite, appearing in granular aggregates (Figure 6g–i).
- (5) The quartz-sulfide stage (V) is the main stage of molybdenite formation, with a large amount of metal sulfide such as pyrite and chalcopyrite formed together with quartz, calcite, fluorite, and other minerals to form various veins, including molybdenite, quartz-molybdenite, quartz-pyrite-chalcopyrite-molybdenite, quartz-pyrite-molybdenite, and quartz-pyrite veins. These veins are filled in the fractures of silicate skarn, hornfels, and granite porphyry (Figure 5e,f).
 - (6) The quartz-carbonate stage (VI) is the final stage of ore formation, characterized by the formation of a large amount of calcite, quartz, pyrite, with minor fluorite (Figure 5f).

4. Sampling and Analytical Methods

4.1. Sampling

Mineralogical analyses of magnetite in this study were conducted on samples primarily collected from the open-pit mining area of the Sandaozhuang tungsten–molybdenum deposit, comprising a total of 9 samples designated as SDZ01–SDZ09. The samples numbered SDZ01–SDZ05 were obtained from granite porphyry closely related to W-Mo mineralization. The SDZ01–SDZ03 granite porphyry has partial silicification alteration signatures, mainly in quartz veins containing minor amounts of pyrite and molybdenite, and potassic alteration occurred in SDZ04 and SDZ05, and K-feldspar-biotite-magnetite veins can be seen interspersed among them. Samples SDZ06–SDZ09 were collected from various types of silicate skarn-type tungsten–molybdenum ores, such as garnet silicate skarn, zoisite-diopside silicate skarn, and wollastonite-silicate skarn. The vein minerals of the three types of silicate skarn ores are primarily composed of garnet, diopside, quartz, wollastonite, epidote, and minor zoisite, whereas metallic minerals are mainly molybdenite, scheelite, magnetite, pyrite, and chalcopyrite.

4.2. EMPA Major Element Analyses

Samples from the Sandaozhuang tungsten–molybdenum deposit were made into probe sections for detailed optical microscope observation and identification of different mineral phases and stages. Target minerals were then selected, and backscattered electron (BSE) imaging was performed after carbon coating. Electron microprobe analyses (EMPAs) were carried out to determine mineral compositions. Backscattering (BSE) and cathodoluminescence (CL) images were obtained using a JXA-8800 instrument (JEOL, Japan) at the Institute of Geology, Chinese Academy of Geological Sciences and China University of Geosciences (Beijing), with a testing acceleration voltage of 20 kV, beam current of 20 nA, and beam spot size of 5 μm .

EMPAs was conducted at the Analysis and Testing Center of the Science Research Institute, China University of Geosciences (Beijing), using a EMPA-1720 electron microprobe analyzer (Shimadzu, Japan). The analyses were performed on an acceleration voltage of 15 kV, a beam current of 10 nA, a beam spot size of 1 μm , and ZAF correction. Following the national standard for electron microprobe analysis, the relative error for the measurement of major elements was managed to be less than 5%.

4.3. LA-ICP-MS Trace Element Analysis

In situ trace element content analysis of minerals was conducted using LA-ICP-MS at the Institute of Mineral Resources, Chinese Academy of Geological Sciences. The GeoLas 2005 laser ablation system (Lambda Physik, Germany) and Agilent 7500a ICP-MS (Agilent Technologies, America) were employed. Helium was used as the carrier gas during the laser ablation process, with a laser frequency of 10 Hz, a beam spot diameter of 50 μm , and an energy density of 5 J/cm². Calibration standards, such as BCR-2G, BIR-1G, and GSE-1G from USGS, were used for calibration [26–29]. For more detailed experimental procedures, please refer to [27].

5. Results

The magnetite occurrences in the Sandaozhuang deposit can be classified into three types, magnetite in granite (Mag1), magnetite in quartz-K-feldspar-biotite veins (Mag2), and magnetite in skarn (Mag3), based on their formation stages. Detailed results of EMPA and LA-ICP-MS for all magnetite samples are summarized in Tables 1 and 2, with the full data supplied in the Supplementary Materials, Tables S1 and S2.

Table 1. Chemical compositions of magnetite from the Sandaozhuang W-Mo deposit (wt%).

Type	Mag1			Mag2			Mag3		
	13	11	20	13	11	20	13	11	20
Number	Min	Max	Mean	Min	Max	Mean	Min	Max	Mean
SiO ₂	0.03	0.88	0.22	0.02	0.66	0.11	0.07	2.28	0.76
TiO ₂	0.04	0.47	0.16	0.02	0.42	0.12	0.00	0.08	0.02
Al ₂ O ₃	0.01	0.29	0.12	0.00	0.18	0.08	0.00	0.14	0.05
FeO _T	91.76	93.67	92.65	91.20	93.21	92.43	87.85	93.37	91.60
MnO	0.00	0.13	0.03	0.00	0.49	0.16	0.36	0.67	0.50
MgO	0.01	0.05	0.02	0.01	0.02	0.01	0.05	0.15	0.06
CaO	0.01	0.06	0.02	0.04	0.13	0.03	0.02	0.49	0.15
Na ₂ O	0.01	0.09	0.04	0.02	0.06	0.03	0.03	0.07	0.03
K ₂ O	0.05	0.17	0.05	0.04	0.04	0.02	0.02	0.05	0.03
Cr ₂ O ₃	0.01	0.13	0.05	0.02	0.14	0.06	0.01	0.13	0.04
V ₂ O ₃	0.30	0.54	0.44	0.01	0.06	0.03	0.01	0.25	0.12
Total	93.41	94.56	93.93	92.73	93.81	93.22	91.48	94.43	93.49

5.1. Major Elements

Based on EMPA analytic results (Table 1, Figure 7), the three types of magnetite are generally characterized by high Ca, Al, Si, and Mn and low Mg, Ti, Na, K, and Cr. The detailed data are presented in the appendix. The FeO_T contents of Mag1 (91.76–93.67 wt%, mean 92.65 wt%) are similar to those of Mag2 (91.20–93.21 wt%, mean 92.43 wt%) and Mag3 (87.85–93.37 wt%, mean 91.60 wt%). However, Mag3 has higher SiO₂ contents (0.07–2.28 wt%, mean 0.76 wt%), MnO contents (0.36–0.67 wt%, mean 0.50 wt%), and CaO contents (0.02–0.49 wt%, mean 0.15 wt%), compared to Mag1 (0.03–0.88 wt% SiO₂; 0–0.13 wt% MnO; 0–0.06 wt% CaO) and Mag2 (0.02–0.66 wt% SiO₂; 0–0.49 wt% MnO; 0–0.13 wt% CaO).

5.2. Trace and Rare Earth Elements

Regarding trace elements (Table 2), all three types of magnetite are depleted in high-field-strength elements (HFSE) including Zr, Hf, Nb, Ta, and Ti, and large ion lithophile elements (LILE) such as Rb, K, Ba, and Sr, relative to the overall composition of the continental crust [30], and enriched in Sn, Mo, V, Cr, Zn, and Ga (Figure 8). The Zn content of Mag1 (222.4–807.4 ppm, mean 448.5 ppm) is comparable to those of Mag2 (326.4–610.6 ppm, mean 402.8 ppm), both of which are higher than those of Mag3 (131.4–435.3 ppm, mean 255.5 ppm). The Ga content of Mag2 (53.1–149.5 ppm, mean 100.7 ppm) is similar to that of Mag1 (24.5–68.9 ppm, mean 41.0 ppm), and both are higher than that of Mag3 (31.3–43.3 ppm, mean 38.7 ppm). The Co content (14.5–298.7 ppm, mean 76.7 ppm), Ge content (4.9–12.2 ppm, mean 8.7 ppm), and Cu content (15.4–264.6 ppm, mean 138.4 ppm) of Mag3 are higher than those of Mag1 and Mag2. Therefore, Mag1 and Mag2 in this deposit are similar to magmatic-type magnetite (a combination of Ni, Cu, Zn, and Ga), while Mag3 is more similar to skarn-type magnetite (with high Co and Ge content) and hydrothermal-type magnetite (with relatively high Cu content).

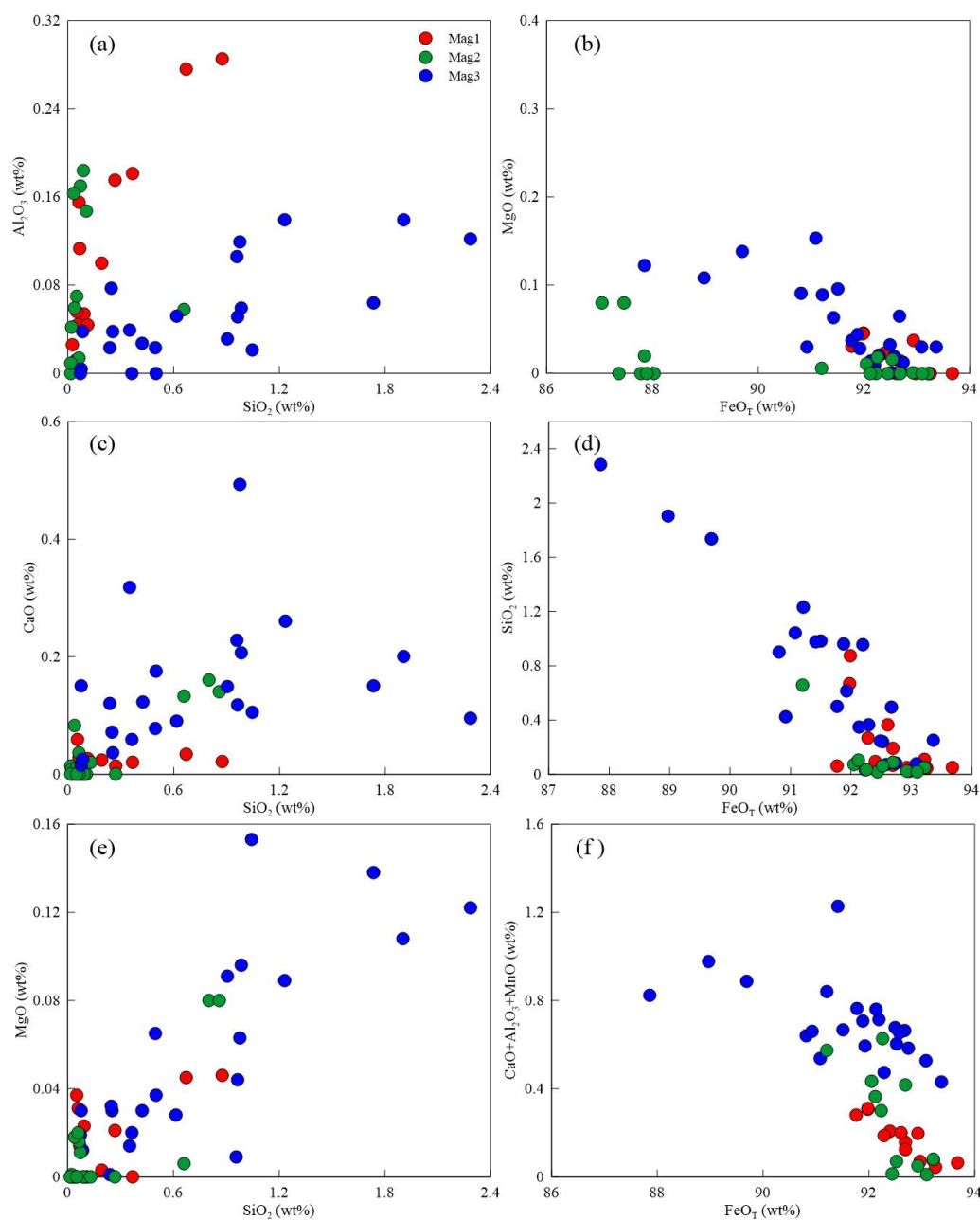


Figure 7. Diagram of major element of magnetite in the Sandaozhuang W-Mo deposit. (a) SiO_2 vs. Al_2O_3 diagram; (b) FeO_T vs. MgO diagram; (c) SiO_2 vs. CaO diagram; (d) FeO_T vs. SiO_2 diagram; (e) SiO_2 vs. MgO diagram; (f) FeO_T vs. $(\text{CaO} + \text{Al}_2\text{O}_3 + \text{MnO})$ diagram.

The ΣREE of all three types of magnetite are relatively low. Mag1 has a higher ΣREE (0.2–34.1 ppm, mean 7.3 ppm) than Mag2 (0.9–14.3 ppm, mean 4.4 ppm) and Mag3 (0.1–5.5 ppm, mean 1.4 ppm). The $(\text{La}/\text{Yb})_N$ ratios (1.0–13.1, mean 4.3) and LREE/HREE ratios (1.9–14.4, mean 7.2) of Mag3 are lower than those of Mag1 (5.2–45.9, mean 15.3; 7.7–19.4, mean 12.6) and Mag2 (3.1–30.2, mean 14.1; 4.5–22.6, mean 15.2). However, all three types have $(\text{La}/\text{Yb})_N$ and LREE/HREE ratios greater than 1, indicating relatively obvious light–heavy rare earth element fractionation. The normalized rare earth element distribution patterns of the chondrite-normalized REE patterns show characteristics of LREE enrichment and HREE depletion (Figure 8).

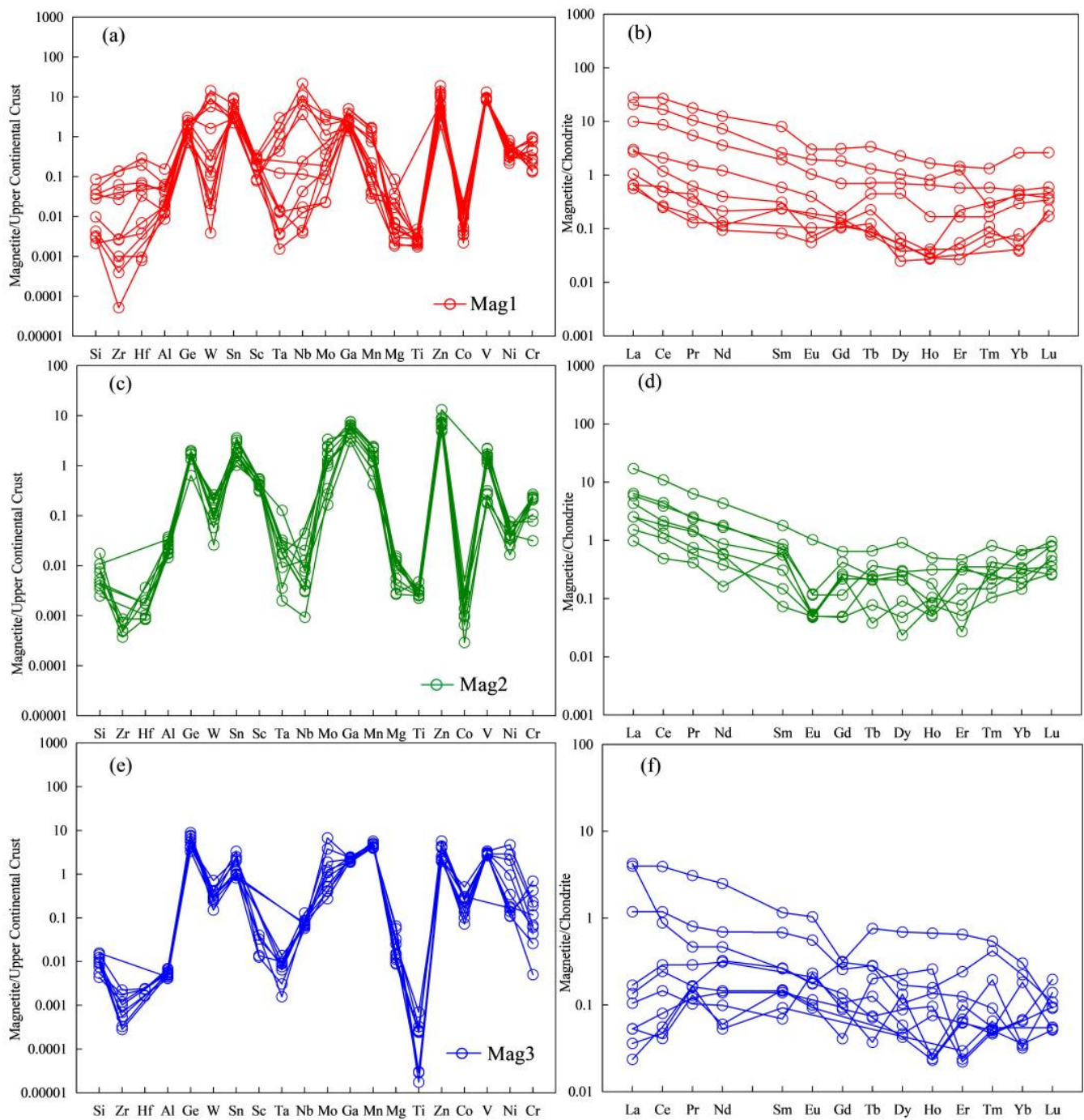


Figure 8. Trace element spider diagram and chondrite-normalized REE patterns of the magnetite in Sandaozhuang MoW deposit (normalized value and arrangement according to [1,30]; chondrite value according to [31]). (a,b) Mag1 in magmatic stage; (c,d) Mag2 in potassic alteration stage; (e,f) Mag3 in retrograde stage.

Table 2. LA-ICP-MS analytic results (ppm) of magnetite from Sandaozhuang W-Mo deposit.

Type	Mag1			Mag2			Mag3		
	10	8	11	10	8	11	10	8	11
Number	Min	Max	Mean	Min	Max	Mean	Min	Max	Mean
Li	0.44	12.72	2.60	0.86	4.56	2.63	0.34	4.07	1.30
B	0.43	4.64	2.02	2.31	6.87	5.20	0.16	10.43	3.28
Sc	1.10	4.76	2.78	4.31	9.65	6.86	0.46	0.95	0.72
V	787.50	1274.32	895.50	21.00	215.51	106.49	256.31	362.04	285.92
Cr	12.20	70.29	33.05	7.19	69.15	22.61	0.15	57.79	17.43
Co	0.38	3.77	1.90	0.11	1.82	0.61	14.51	298.72	77.69
Ni	10.21	37.73	22.09	0.78	9.01	2.95	5.12	220.71	36.01
Cu	0.13	23.78	6.75	0.26	5.02	1.32	15.41	264.60	138.38
Zn	222.39	807.39	448.50	326.37	610.59	402.82	131.44	435.30	255.50
Ga	24.45	68.92	40.97	53.13	149.48	100.72	31.26	43.28	38.65
Ge	1.00	4.32	2.31	1.90	3.57	2.36	4.90	12.21	8.68
As	7.57	15.52	10.66	3.37	7.79	6.16	2.47	13.55	8.03
Rb	0.09	4.08	1.61	0.35	1.85	0.97	0.16	17.57	3.23
Sr	0.13	87.76	10.63	0.30	4.12	1.28	0.36	24.62	5.53
Y	0.03	20.18	3.18	0.12	0.74	0.34	0.05	1.45	0.30
Zr	0.08	26.55	7.47	0.07	11.74	2.73	0.13	9.83	2.02
Nb	0.05	92.76	24.31	0.04	4.10	0.92	0.76	1.25	0.99
Mo	0.54	3.92	1.94	1.23	8.54	3.57	0.20	2.09	1.12
Cd	0.15	0.85	0.41	0.25	0.69	0.47	0.21	1.22	0.62
In	0.00	0.44	0.08	0.02	0.36	0.12	0.01	0.78	0.18
Sn	4.70	13.81	8.57	2.14	8.82	4.94	1.73	14.45	5.12
Sb	0.06	1.00	0.31	0.04	0.96	0.26	0.10	0.78	0.40
Cs	0.01	6.53	0.84	0.00	0.08	0.03	0.03	24.59	3.73
Ba	0.45	17.28	3.20	1.71	9.02	4.48	0.84	35.12	10.12
Hf	0.01	1.54	0.42	0.00	0.09	0.03	0.01	0.23	0.07
Ta	0.00	2.69	0.53	0.02	0.11	0.04	0.00	0.03	0.01
W	0.04	4.00	1.13	1.30	6.82	3.15	0.40	1.67	0.86
Tl	0.01	0.57	0.11	0.00	0.01	0.01	0.00	0.43	0.09
Pb	0.07	89.84	19.06	0.42	6.32	1.99	3.14	21.23	8.63
Bi	0.01	0.61	0.12	0.00	0.22	0.06	1.57	36.05	12.69
Th	0.02	66.69	12.62	0.05	1.37	0.40	0.01	0.33	0.09
U	0.00	94.76	13.35	0.01	0.86	0.18	0.05	13.46	2.10
La	0.04	6.59	1.23	0.23	4.05	1.19	0.01	1.00	0.24
Ce	0.09	16.36	2.75	0.30	6.67	1.95	0.02	2.40	0.53
Pr	0.01	1.70	0.28	0.04	0.60	0.18	0.00	0.29	0.07
Nd	0.03	5.86	0.95	0.08	2.03	0.59	0.02	1.17	0.31
Sm	0.01	1.23	0.22	0.01	0.28	0.09	0.01	0.21	0.07
Eu	0.00	3.27	0.51	0.00	0.06	0.01	0.00	0.07	0.02
Gd	0.02	39.73	5.80	0.01	0.13	0.05	0.02	0.23	0.06
Tb	0.00	4.14	0.54	0.00	0.02	0.01	0.00	0.03	0.01
Dy	0.01	26.63	2.76	0.01	0.23	0.07	0.01	0.18	0.05
Ho	0.00	6.54	0.67	0.00	0.03	0.01	0.00	0.04	0.01
Er	0.00	21.49	3.13	0.00	0.08	0.03	0.00	0.11	0.03
Tm	0.00	3.94	0.50	0.00	0.02	0.01	0.00	0.01	0.00
Yb	0.01	32.14	3.28	0.02	0.11	0.06	0.01	0.08	0.03
Lu	0.00	5.89	0.75	0.01	0.02	0.01	0.00	0.01	0.00
ΣREE	0.19	34.13	7.34	0.91	14.32	4.38	0.08	5.52	1.37
LREE	0.17	31.91	6.89	0.75	13.68	4.12	0.05	5.04	1.21
HREE	0.02	2.22	0.45	0.08	0.64	0.26	0.01	0.60	0.16
LREE/HREE	7.73	19.39	12.59	4.51	22.61	15.16	1.88	14.41	7.15
La _N /Yb _N	5.20	45.94	15.30	3.08	30.16	14.07	1.02	13.11	4.31
δEu	0.32	1.02	0.70	0.11	0.84	0.38	0.00	3.95	1.43
δCe	0.63	1.27	0.95	0.70	1.03	0.88	0.38	1.62	1.07

Note: The units for trace and rare earth element mass fractions are 10^{-6} . The values for chondrite normalization are from [31]. $\delta\text{Eu}_N = 2\text{Eu}_N / (\text{Sm}_N + \text{Gd}_N)$ and $\delta\text{Ce}_N = 2\text{Ce}_N / (\text{La}_N + \text{Pr}_N)$.

6. Discussion

6.1. Origin of Magnetite

The significant variations in Al_2O_3 , MnO , CaO , MgO , TiO_2 , Ni , Cr , V , and Ga contents in magnetite are important indicators for the different types and mineralization stages of magnetite [1,2,32–36]. Mag1 mainly falls within the porphyry field, Mag2 mainly falls within the skarn porphyry region, and Mag3 mainly falls within the skarn region in the compositional diagrams of TiO_2 - Al_2O_3 - $(MgO + MnO)$, $(Ti + V)$ vs. $(Ca + Al + Mn)$, $(Ti + V)$ vs. $(Al + Mn)$, and $(Ti + V)$ vs. $Ni/(Cr + Mn)$ (Figure 9). This observation is corresponding to the petrographic observations, which revealed that Mag1 is present in quartz and feldspar phenocrysts in granite porphyry, Mag2 in K-feldspar-black biotite veins cutting granite porphyry, and Mag3 is associated with skarn minerals such as diopside, garnet, tremolite, and actinolite.

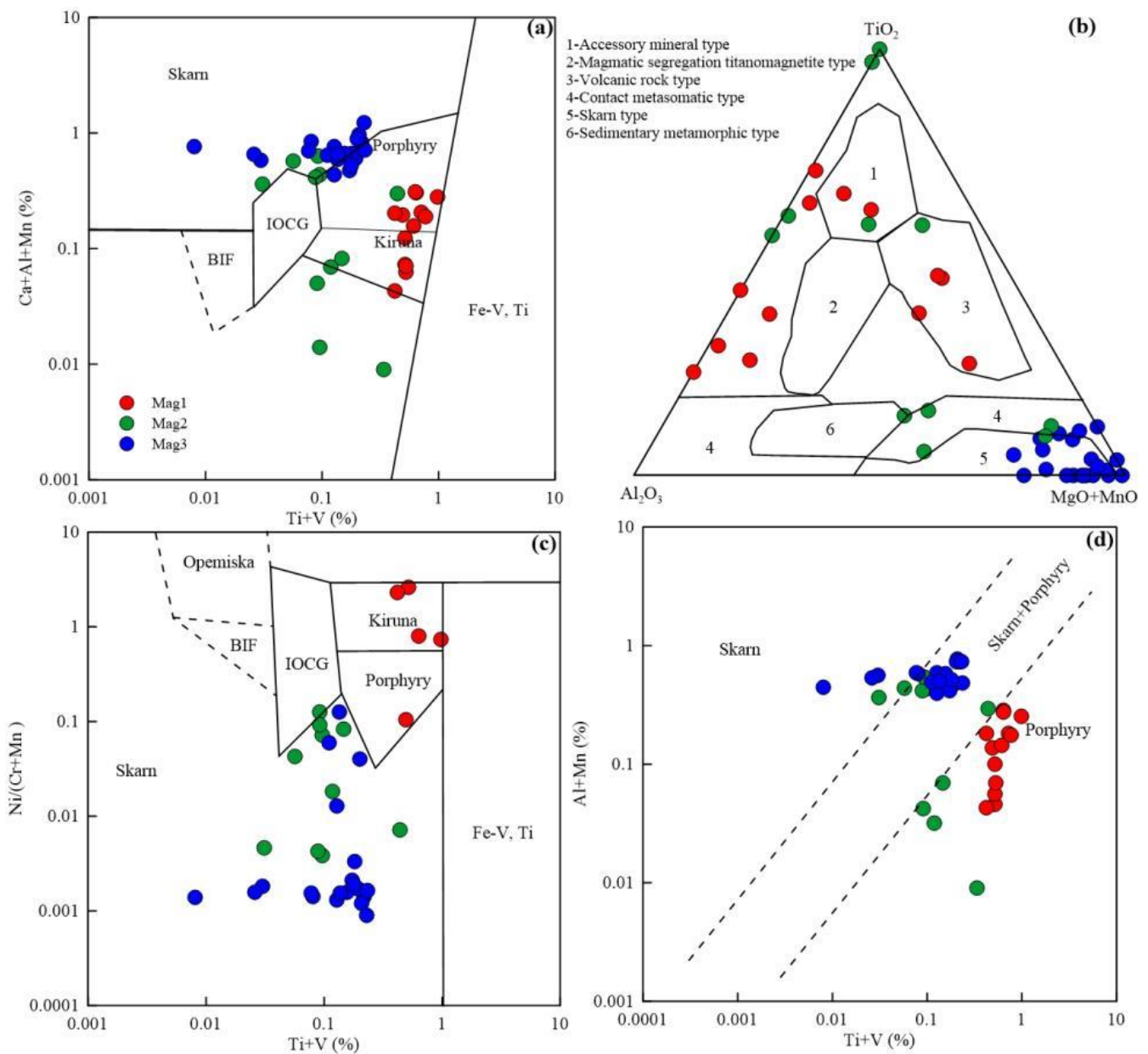


Figure 9. Magnetite genetic classification diagrams (a), $(Ti + V)$ vs. $(Ca + Al + Mn)$ discrimination diagram after [1]; (b), ternary TiO_2 - Al_2O_3 - $(MgO + MnO)$ discrimination diagram after [32]; (c,d), $(Ti + V)$ vs. $(Al + Mn)$ and $(Ti + V)$ vs. $Ni/(Cr + Mn)$ after [33]).

Ni and Cr exhibit coupled geochemical behavior in silicate magmas, with Cr having a higher solubility than Ni under high-temperature conditions, resulting in a Ni/Cr ratio of ≤ 1 for magnetite in magmatic rocks. Experimental studies by [37] supported this observation. However, during (magmatic) hydrothermal activity, Ni and Cr show a distinct decoupling behavior, with Ni having a much higher solubility than Cr, resulting in a magnetite Ni/Cr ratio of ≥ 1 for hydrothermal deposits. The combination of Ni/Cr and Ti ratios has been used to distinguish between magmatic and hydrothermal magnetite deposits [2,36]. However, the various magnetite types in the Sandaozhuang deposit exhibit different geochemical characteristics. Data from Sandaozhuang show that Mag1 (with a Ti concentration of up to 2863 ppm) and Mag2 (with a Ti concentration of up to 1716 ppm) have high Ti contents, consistent with the published data that magmatic magnetite has a higher Ti content than hydrothermal magnetite [1,38] (Figure 10a). Additionally, most of the Mag1 and Mag2 samples fall into the magmatic magnetite field (Figure 10b), while Mag3 falls into the hydrothermal magnetite field. Therefore, we suggest that Mag1 has a magmatic origin, Mag2 has a magmatic-hydrothermal origin, and Mag3 is formed by metasomatism of the ore-forming fluids, and hence falls in the hydrothermal category.

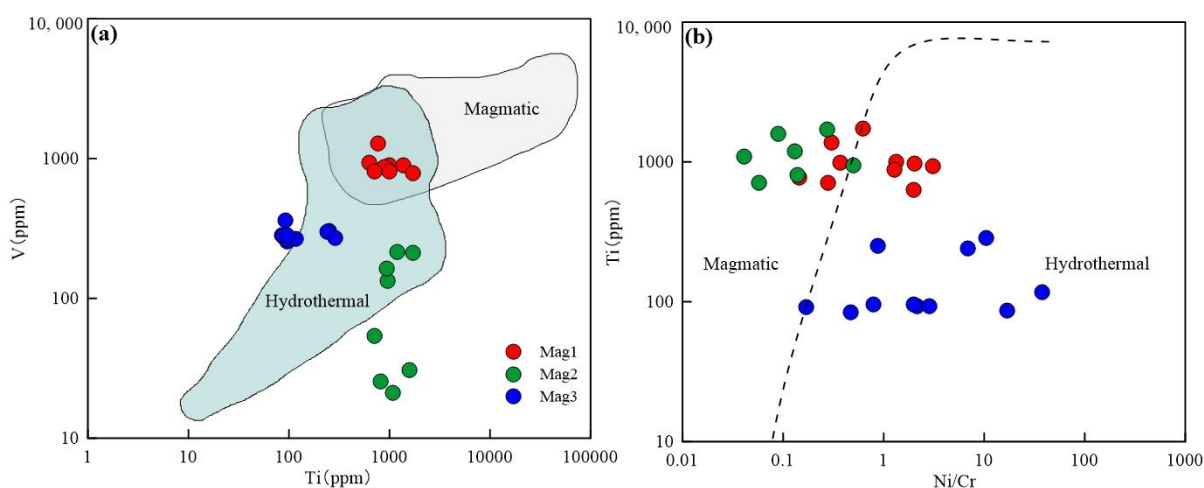


Figure 10. Genetic discrimination diagrams of (a) Ti vs. V and (b) Ni/Cr vs. Ti (fields of magmatic and hydrothermal magnetite being from [1] and [38]).

6.2. Element Behavior of Magnetite during Skarn Formation

Magnetite formed in different types of deposits can incorporate various trace elements, and its composition is controlled by multiple factors, including the composition and physicochemical parameters of the ore-forming fluids, such as temperature, pressure, cooling rate, oxygen fugacity, sulfur fugacity, as well as water–rock reactions and coexisting minerals [1,5,33]. Although each element's abundance may be influenced by several factors, some elements exhibit regular variations between magnetite formed at different stages of mineralization [2,4,35]. Therefore, distinct elements such as Al, Mn, Mg, Ti, V, Cr, Ga, and Sn, which are closely related to the oxygen fugacity and temperature of the ore-forming fluids by the compositions of magnetite formed at different mineralization stages, are used for inferring the evolution of ore-forming fluids [1,2,5,33,39–41].

A previous study has demonstrated that the Cr and V contents in magnetite exhibit a negative correlation with oxygen fugacity, and a decrease in the former indicates an increase in oxygen fugacity [5,40,42–46]. Numerous analogous reports have been documented [9,11–13,45,47]. Mag1 has high concentrations of Cr (mean: 33.05 ppm) and V (mean: 895.50 ppm); however, Mag2 and Mag3 are characterized by low contents of Cr (mean: 22.61 ppm; 17.43 ppm) and V (mean: 106.49 ppm; 285.92 ppm) in the Sandaozhuang W-Mo deposit, indicating a consistent trend of a slight initial decrease followed by an increase in Cr and V contents from Mag1 to Mag2 and then to Mag3 (Figure 11), and a minor increase in the oxygen fugacity of the ore-forming fluids from the magmatic stage

to the potassic stage, followed by a significant decrease from the potassic stage to the late skarn stage.

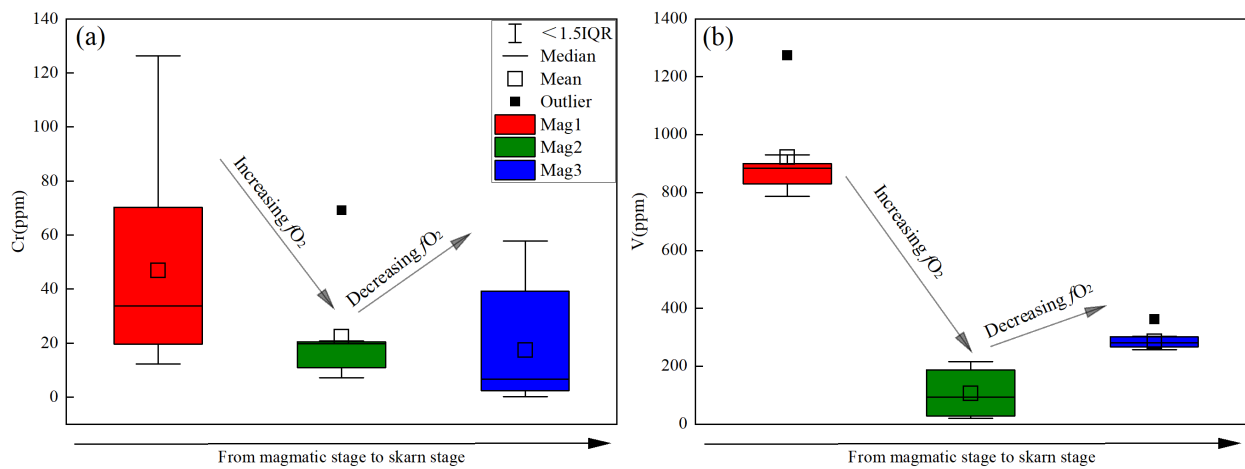


Figure 11. Chromium (a) and vanadium (b) distribution in magnetite showing fO_2 changes in the ore-forming fluid from different ore formation stages in the Sandaozhuang deposit.

Some researchers have used Fe-Ti oxides as an oxygen barometer, which has been widely applied in igneous and metamorphic rocks [1,33,48]. At different temperatures, the minimum oxygen fugacity at which magnetite is stable is iron-magnetite (IM) or magnetite-wustite (MW) phase assemblages. The fayalite-magnetite-quartz (FMQ) buffer indicates the minimum oxygen fugacity at which iron is mainly present in the form of magnetite. If the oxygen fugacity is lower than that of the FMQ buffer, iron will mainly enter the ferrosilicate minerals. The upper limit of oxygen fugacity at which magnetite is stable is hematite-magnetite (HM), and as oxygen fugacity continues to increase, magnetite will transform to hematite (Figure 12). A study on the Sandaozhuang deposit’s three types of magnetite has uncovered that Mag1 is frequently associated with ilmenite during the magma stage (Figure 6c), while Mag2 is typically related to small quantities of hematite during the potassic alteration stage (Figure 6f). During the retrograde alteration stage, Mag3 mainly coexisted with sulfides (e.g., chalcopyrite, molybdenite) and ferrosilicate minerals (e.g., garnet, actinolite) (Figure 6h,i). These observations suggest that the fluid oxygen fugacity increases to a small extent from the magma stage to the potassic alteration stage, and then decreases significantly from the potassic alteration stage to the late-stage skarn stage.

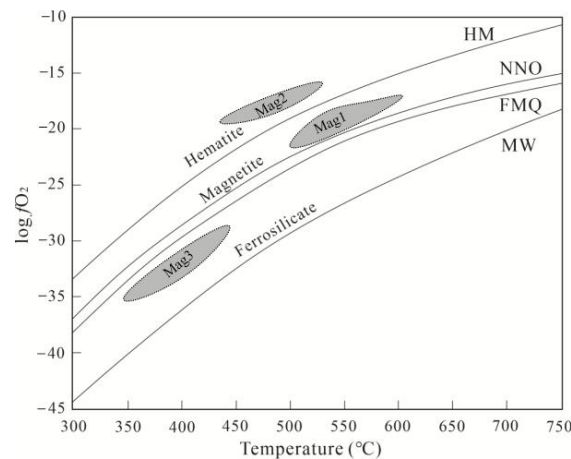


Figure 12. Redox buffers in the Fe-Si-O system and the $\log fO_2$ -T relationship diagram (after [48]). Abbreviations are the fugacity buffers: HM, hematite-magnetite; NNO, nickel-nickel oxide; FMQ, fayalite-magnetite-quartz; MW, magnetite-wustite.

Temperature condition plays a critical role in determining the distribution of elements in minerals, with higher temperatures facilitating the incorporation of elements into mineral lattices and lower temperatures hindering element enrichment [49]. The decrease in the contents of compatible elements such as Al, Mn, Mg, V, Ga, and Sn in magnetite with decreasing temperature is an important feature of the transformation from magmatic to hydrothermal magnetite [2]. The concentration of Ti in magnetite in magmatic-hydrothermal systems is controlled by temperature [8]. During the formation of magnetite, Ti typically replaces Fe^{3+} in the lattice of magnetite, and the temperature of magnetite formation is positively correlated with Ti content, making Ti a reliable indicator of magnetite formation temperature [1,2,50]. The previous study showed that the solubility of Al and Ti in magnetite reflects a positive dependence on temperature [6,51]. Additionally, V may be controlled not only by oxygen fugacity but by the temperature of the hydrothermal environment [8,40], which is consistent with the positive correlation between V and Ti content in magnetite from the Sandaozhuang deposit. As shown in Figure 13, the contents of Al, Ga, and Sn progressively decrease from Mag1 to Mag3, while Mn and Mg exhibit a negative correlation, which may be related to changes in oxygen fugacity. Combined with the data points in (Ti + V) vs. (Al + Mn) diagram that are correlated with temperature [2], the temperature of magnetite gradually decreased from Mag1 to Mag3, with formation temperatures in the range of 300–600 °C for Mag1, Mag2, and Mag3, consistent with the trend of magma evolution during skarn mineralization process, comparable to the previous fluid inclusion studies [15].

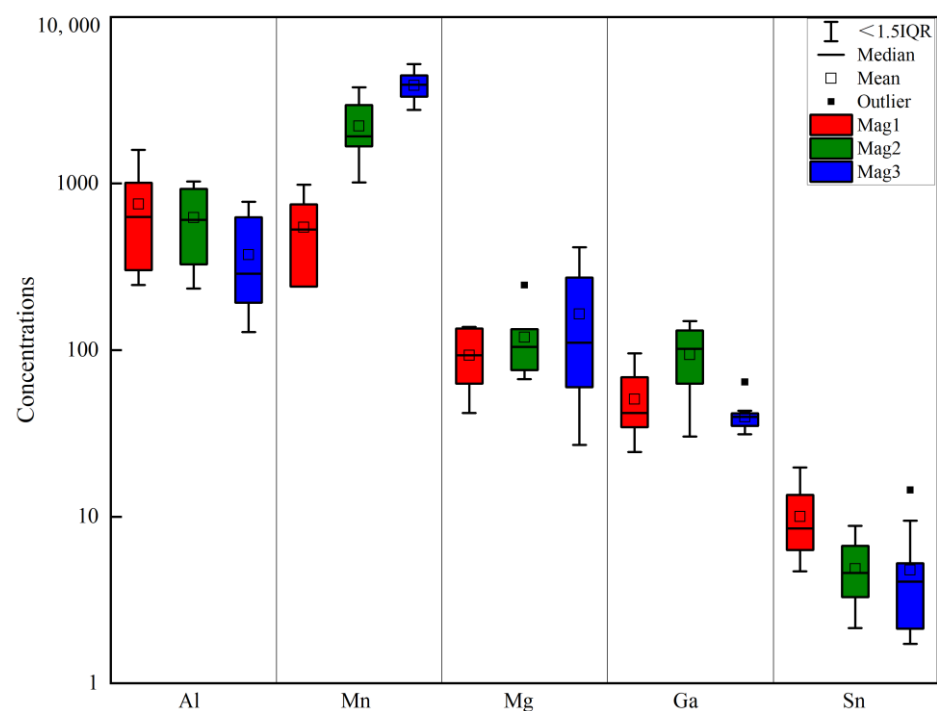


Figure 13. Comparative box plot of Al, Mn, Mg, Ga, and Sn concentrations of the different magnetite types/generations.

It is widely accepted that co-precipitated minerals can affect the trace element composition of magnetite due to differing distribution coefficients between magnetite and coexisting minerals [1]. Co, Ni, Cu, Zn, and Bi are chalcophile elements that are more effectively competed by sulfides than oxides. Therefore, if magnetite particles precipitated from fluids enriched in these elements are associated with sulfides, their concentrations are typically lower [1,40]. In this study, changes in Co, Ni, Cu, and Bi in magnetite during the magmatic to potassic alteration stages followed this pattern. As shown in Figure 13, the concentrations of Co, Ni, Cu, and Bi in magnetite gradually decreased from Mag1 to Mag2,

consistent with the genetic model of increasing sulfides in the mineralization. However, in Mag3, which coexists with sulfides, the expected depletion of Co, Ni, Cu, and Bi was not observed, ruling out the possibility of co-extraction with sulfide minerals, although Zn did show a significant loss in magnetite (Figure 14). To explain this contradiction, it is speculated that the lack of depletion of Co, Ni, Cu, and Bi in Mag3 may be caused by the earlier precipitation of magnetite, which is supported by the partial replacement of magnetite by sulfides (Figure 6h,i), similar to the Fe-Cu deposits in the Kangdian metallogenic province, China [5]. Since magnetite may have crystallized before sulfides, the depletion of Zn in magnetite is unlikely to be caused by coexisting sulfides, indicating that hydrothermal reactivation allows Zn to preferentially dissolve over other trace elements in the iron-rich hydrothermal fluids [40]. Based on the uneven contact or local replacement vein structure formed by Mag3 and surrounding chalcopyrite (Figure 6i), the hydrothermal reactivation of Zn may have occurred during this stage; however, the possibility of later hydrothermal alteration stages such as chloritization and carbonatization could not be completely ruled out.

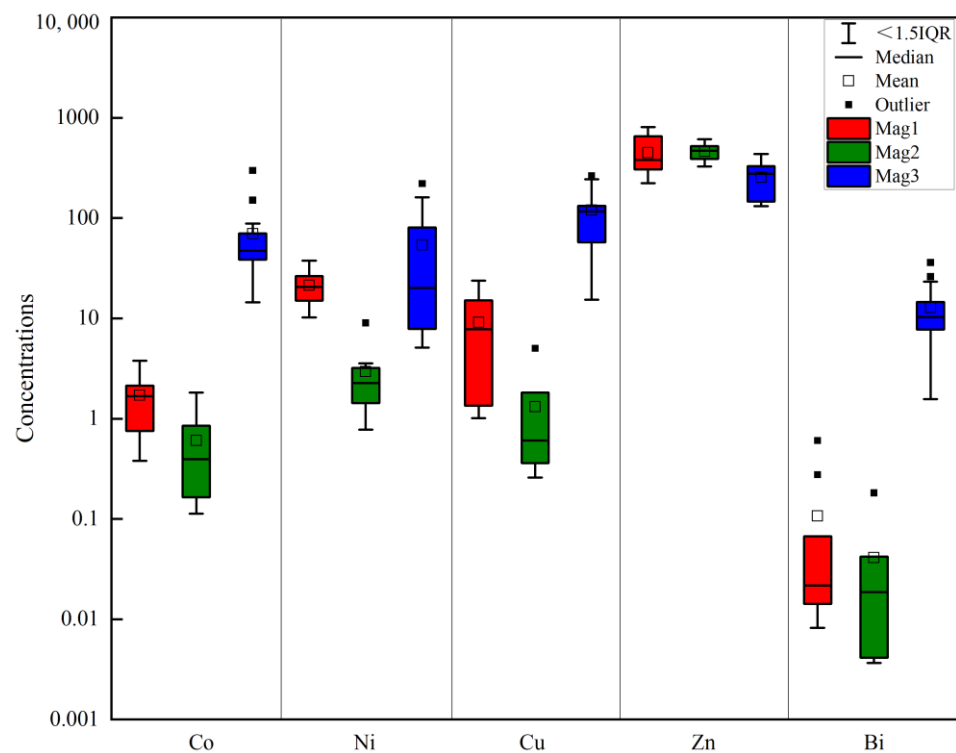


Figure 14. Comparative box plot of Co, Ni, Cu, Zn, and Bi concentrations of the different magnetite types and generations.

6.3. Constraints to Metallogenic Mechanism from Compositional Change of Magnetite

The multi-element diagram of trace elements in magnetite is a valuable tool for investigating the genesis and evolution of mineral deposits [1,2,33]. In addition, FeO_T is approximately inversely proportional to SiO_2 , MgO , and $\text{MnO} + \text{CaO} + \text{Al}_2\text{O}_3$. SiO_2 and MgO show different trends in Mag1, Mag2, and Mag3 (Figure 8). These observations suggest the existence of extensive water–rock interaction and material exchange between the mineralizing fluids and the surrounding carbonate rocks (containing such as Ca, Mn, Mg) and host rocks of granite (Si, Al), with enrichment in the mineralizing fluids during the skarn stage, particularly the generation of large amounts of diopside and garnet, resulting in Mag3 having higher Si, Ca, and Mn than Mag1 and Mag2 (Figure 8). Al, Sc, Ti, V, Nb, and Hf are relatively depleted, while Zr, Hf, Nb, Ta, Ti, V, and other HFSE elements show similar linear variation characteristics during the evolution from Mag1 to Mag3 (Figure 8), indicating consistent material sources [4]. Y^{3+} (1.019 Å) and Ho^{3+} (1.015 Å) possess the

same ionic valence [52] and almost identical 8-fold coordinated ionic radii, suggesting that Y and Ho have similar geochemical behaviors [53,54]. The relatively uniform Y/Ho ratios of the three types of magnetite in the Sandaozhuang deposit are consistent with those of the Nanlinghu granite (Figure 15), indicating that the ore-forming material of the magnetite mainly comes from magmatic sources. This finding is in line with studies of the C-O-H isotope [25] and scheelite [16], which both suggest that the ore-forming material of the Sandaozhuang deposit is primarily derived from magmatic sources.

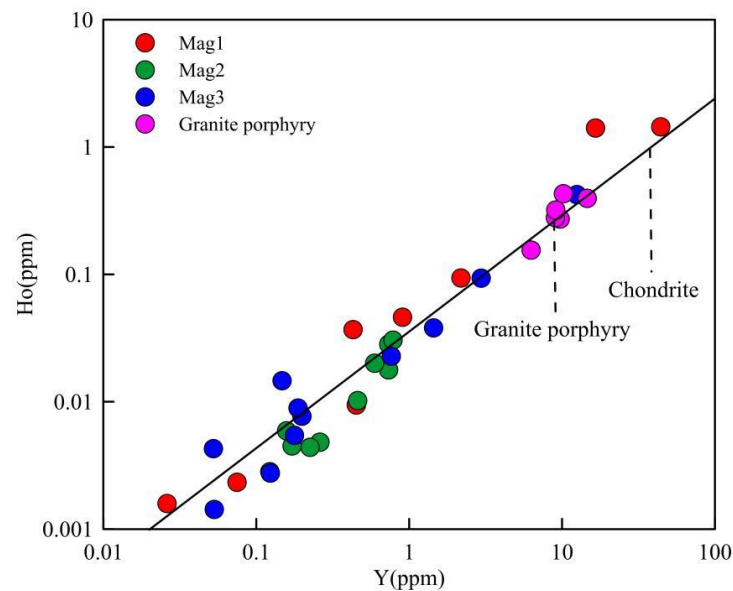


Figure 15. Ho-Y diagram of magnetite in the Sandaozhuang MoW deposit. Notes: Chondrite line is from [54] and Ho/Y ratio of granite porphyry is from [55].

Magmatic fluids are typically characterized by low REE contents, LREE enrichment, HREE depletion, and variable Eu anomalies [56–62]. An increase in the salinity of hydrothermal fluids can enhance the distribution coefficient of REEs into the fluid phase and reduce Eu anomalies. The magnitude of REE fractionation is strongly influenced by the pH of hydrothermal fluids [47,53,63]. At mildly acidic conditions, fluids are typically enriched in LREE, depleted in HREE, and characterized by negative Eu anomalies [53]. In contrast, near-neutral fluids are enriched in HREE, depleted in LREE, and exhibit positive or no Eu anomalies [47,63]. Moreover, REE³⁺ and Y preferentially coordinate with “hard” acids (such as OH[−], CO₃^{2−}, F[−]), while Eu²⁺ behaves like an alkaline earth metal such as Ca²⁺ and can migrate with Cl[−] to form stable EuCl₄^{2−} complexes, resulting in a pronounced positive Eu anomaly [63–65]. The REE partitioning patterns of Mag1 and Mag2 in the skarn stage of the Sandaozhuang deposit show significant LREE enrichment, HREE depletion, and negative Eu anomalies (Figure 8), indicating that they crystallized from mildly acidic and high salinity fluids with magmatic characteristics. In contrast, Mag3 in the retrograde alteration stage shows slight LREE depletion, slight HREE enrichment, and a positive Eu anomaly (Figure 8). This REE distribution pattern may be influenced by early crystallization of skarn minerals [9,18], suggesting that the fluid in this stage may have inherited the characteristics of the late-stage fluid in the skarn stage, which was characterized by a medium-acidic and low-salinity fluid. This argument is similar to the results [15,24], which indicate that the early stage fluid of the Sandaozhuang deposit had magmatic-hydrothermal characteristics with high temperature and high salinity, while the late-stage fluid had characteristics of low temperature and low salinity.

In magmatic-hydrothermal systems, changes in the physical conditions of ore-forming fluids such as temperature, pressure, and solubility, as well as reactions with the surrounding rocks or interactions with other fluids, can cause the precipitation of metal elements. Oxygen fugacity and temperature play a crucial role in the solubility and stability of metal

complexes in fluids [66]. Variations in V, Cr, and Ti in magnetite (Figure 11) suggest a continuous decrease in temperature from the magmatic stage to the potassic alteration stage, and then to the late-stage skarn stage, while oxygen fugacity initially increased and then decreased. However, this study argued that increased oxygen fugacity during the early potassic alteration stage facilitated further enrichment of W and Mo in the fluid, as reflected in the variations in Mo and W contents in magnetite at different stages. From the magmatic stage to the potassic alteration stage and then to the late-stage skarn stage, the Mo and W contents in magnetite first increased and then decreased significantly (Figure 16). This may be related to the high temperature and oxygen fugacity of the early ore-forming fluid, where ore-forming elements S, Mo, and W (S^{6+} , S^{4+} , Mo^{6+} , W^{6+}) can migrate in solution in forms of sulfides, halides, and soluble complexes. In the later stages of retrograde alteration, the water–rock reaction was relatively strong, leading to a gradual decrease in fluid temperature and oxygen fugacity, which reduced the solubility of Mo and W. Additionally, boiling of the fluid and mixing with atmospheric water caused a rapid change in fluid properties (Figure 17) [15,24], resulting in the crystallization of molybdenite and scheelite and a subsequent decrease in the ionic concentrations of Mo and W from the ore-forming fluid.

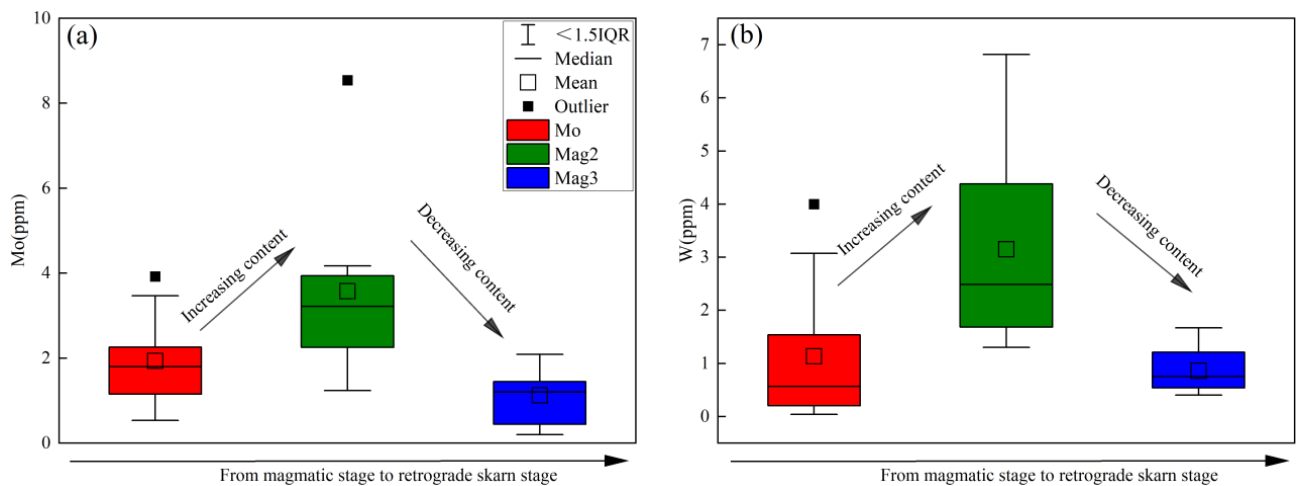


Figure 16. Diagrams of (a) Mo and (b) W content changes in magnetite at different stages in the Sandaozhuang molybdenum–tungsten deposit.

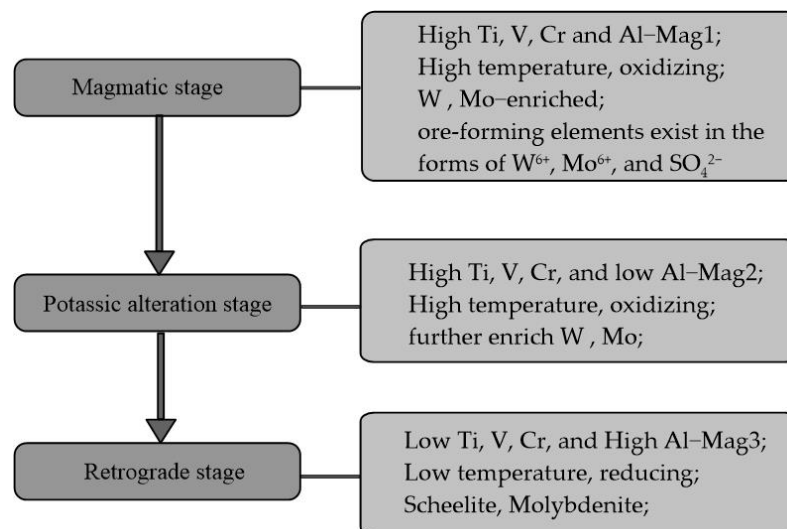


Figure 17. Evolution diagram of fluid properties of magnetite at different stages from Sandaozhuang deposit.

7. Conclusions

Through the above study, the main conclusions are as follows.

- (1) The magnetite in the Sandaozhuang deposit can be classified into three types: magmatic magnetite (Mag1), magmatic-hydrothermal magnetite (Mag2), and hydrothermal magnetite (Mag3). All three types of magnetite are depleted in high-field-strength elements (HFSEs) such as Zr, Hf, Nb, Ta, and Ti, as well as large-ion lithophile elements (LILEs) such as Rb, K, Ba, and Sr, and enriched in Sn, Mo, V, Cr, Zn, and Ga relative to the overall continental crust composition. Mag3 does not exhibit depletion in Co, Ni, Cu, and Bi, suggesting that magnetite precipitation occurred slightly earlier than sulfides. The depletion of Zn in Mag3 implies that Zn was extracted by later hydrothermal fluids during the same stage, indicating limited influence of coexisting sulfides on the composition of magnetite in the Sandaozhuang deposit.
- (2) Mag1, Mag2, and Mag3 show similar trace element spider and rare earth element distribution patterns, in addition to Y/Ho ratios, indicating a consistent magmatic source.
- (3) The changes in V and Cr contents in magnetite, and the (Ti + V) and (Al + Mn) values, reflect the evolution of oxygen fugacity (increasing from Mag1 to Mag2 and decreasing from Mag2 to Mag3) and temperature (decreasing from Mag1 to Mag3) during the skarn mineralization process. The early high-temperature and high-oxygen-fugacity magmatic fluids further enriched W and Mo in the hydrothermal fluids. The rapid change in fluid properties during the retrograde alteration stage resulted in the precipitation of scheelite and molybdenite.

Supplementary Materials: The following supporting information can be downloaded at: <https://www.mdpi.com/article/10.3390/min13081091/s1>, Table S1: Major compositions of magnetite from the Sandaozhuang W-Mo deposit, Table S2: Trace Element compositions of magnetite from the Sandaozhuang W-Mo deposit.

Author Contributions: Conceptualization: Z.Z. and Z.L.; experiments: Z.Z.; data curation: Z.Z. and L.C.; methodology: Z.L. and Z.Z.; investigation: Q.G., U.S. and Y.C.; resources: Z.L.; writing—original draft preparation: Z.Z.; writing—review and editing: Z.L., U.S. and L.C.; visualization: Z.Z.; project administration: Z.L. and M.S.; funding acquisition: Z.L. and M.S. All authors have read and agreed to the published version of the manuscript.

Funding: This research was funded by the National Natural Science Foundation of China (41872092), Qianjiangyuan Baishanzu National Park-Baishanzu administration (2021ZDZX03) and the Power China Huadong Engineering Corporation (20220795).

Data Availability Statement: Not applicable.

Acknowledgments: The authors thank Q. Wang, Z.Y. Chen, and B. Shi from the Institute of Mineral Resources, Chinese Academy of Geological Sciences, for their assistance with EMAP and LA-ICP-MS analysis and BSE work.

Conflicts of Interest: The authors declare no conflict of interest.

References

1. Dare, S.A.S.; Barnes, S.-J.; Beaudoin, G.; Méric, J.; Boutroy, E.; Potvin-Doucet, C. Trace elements in magnetite as petrogenetic indicators. *Miner. Depos.* **2014**, *49*, 785–796. [[CrossRef](#)]
2. Nadoll, P.; Angerer, T.; Mauk, J.L.; French, D.; Walshe, J. The chemistry of hydrothermal magnetite: A review. *Ore Geol. Rev.* **2014**, *61*, 1–32. [[CrossRef](#)]
3. Barnes, S.J.; Roeder, P.L. The Range of Spinel Compositions in Terrestrial Mafic and Ultramafic Rocks. *J. Petrol.* **2001**, *42*, 2279–2302. [[CrossRef](#)]
4. Nadoll, P.; Koenig, A.E. LA-ICP-MS of magnetite: Methods and reference materials. *J. Anal. Atom. Spectrom.* **2011**, *26*, 1872–1877. [[CrossRef](#)]
5. Chen, W.T.; Zhou, M.-F.; Gao, J.-F.; Hu, R. Geochemistry of magnetite from Proterozoic Fe-Cu deposits in the Kangdian metallogenic province, SW China. *Miner. Depos.* **2015**, *50*, 795–809. [[CrossRef](#)]
6. Hu, H.; Lentz, D.; Li, J.W.; McCarron, T.; Zhao, X.F.; Hall, D. Re-equilibration processes in magnetite from iron skarn deposits. *Econ. Geol.* **2014**, *110*, 1–8. [[CrossRef](#)]

7. Chen, H.; Han, J. Study of Magnetite: Problems and Future. *Bull. Mineral. Petrol. Geochem.* **2015**, *34*, 724–730.
8. Canil, D.; Grondahl, C.; Lacourse, T.; Pisiak, L.K. Trace elements in magnetite from porphyry Cu-Mo-Au deposits in British Columbia, Canada. *Ore Geol. Rev.* **2016**, *72*, 1116–1128. [[CrossRef](#)]
9. Ding, T.; Ma, D.; Lu, J.; Zhang, R. Magnetite as an indicator of mixed sources for W-Mo-Pb-Zn mineralization in the Huangshaping polymetallic deposit, southern Hunan Province, China. *Ore Geol. Rev.* **2018**, *95*, 65–78. [[CrossRef](#)]
10. Zhao, Z.H.; Yan, S. Minerals and relevant metallogeny and exploration. *Acta Petrol. Sin.* **2019**, *35*, 31–68.
11. Liu, Y.; Fan, Y.; Zhou, T.; Xiao, X.; White, N.C.; Thompson, J.; Hong, H.; Zhang, L. Geochemical characteristics of magnetite in Longqiao skarn iron deposit in the Middle-Lower Yangtze Metallogenic Belt, Eastern China. *Miner. Depos.* **2019**, *54*, 1229–1242. [[CrossRef](#)]
12. Wu, C.; Chen, H.; Hong, W.; Li, D.; Liang, P.; Fang, J.; Zhang, L.; Lai, C. Magnetite chemistry and implications for the magmatic-hydrothermal ore-forming process: An example from the Devonian Yuleken porphyry Cu system, NW China. *Chem. Geol.* **2019**, *522*, 1–15. [[CrossRef](#)]
13. Guo, J.-H.; Leng, C.-B.; Zhang, X.-C.; Zafar, T.; Chen, W.T.; Zhang, W.; Tian, Z.-D.; Tian, F.; Lai, C.-K. Textural and chemical variations of magnetite from porphyry Cu-Au and Cu skarn deposits in the Zhongdian region, northwestern Yunnan, SW China. *Ore Geol. Rev.* **2020**, *116*, 103245. [[CrossRef](#)]
14. Xiang, J.P.; Pei, R.F.; Xing, B.; Wang, C.Y.; Tian, Z.H.; Chen, X.D.; Ye, H.S.; Wang, H.L. The formation process and Mo (W) mineralization of the skarn in the Nannihu-Sandaozhuang Mo (W) deposit. *Geol. China* **2016**, *43*, 2131–2153.
15. Shi, Y.L.; Li, N.; Yang, Y. Ore geology and fluid inclusion geochemistry of the Sandaozhuang Mo-W deposit in Luanchuan county, Henan province. *Acta Petrol. Sin.* **2009**, *25*, 2575–2587.
16. Zhan, Q.; Gao, X.Y.; Meng, L.; Zhao, T.P. Ore genesis and fluid evolution of the Sandaozhuang supergiant W-Mo skarn deposit, southern margin of the North China Craton: Insights from scheelite, garnet and clinopyroxene geochemistry. *Ore Geol. Rev.* **2021**, *139*, 104551. [[CrossRef](#)]
17. Meinert, L.D. Skarns and skarn deposits. *Geosci. Can.* **1992**, *19*, 145–162.
18. Nie, X.; Yi, J.W.; Chen, P.P.; Wang, M.Y.; Yan, X.G.; Hou, F.J.; Zhang, S.T.; Li, L. Skarn mineral characteristics of Sandaozhuang Mo-W deposit and their geological significance. *J. Chin. Electron Microsc. Soc.* **2014**, *33*, 108–116.
19. Chen, Y.F.; Fu, S.G.; Qiang, L.Z. The tectonic environment for the formation of the Xionger Group and the Xiyanghe Group. *Geol. Rev.* **1992**, *38*, 325–333.
20. Mao, J.W.; Pirajno, F.; Xiang, J.F.; Gao, J.J.; Ye, H.S.; Li, Y.F.; Guo, B.J. Mesozoic molybdenum deposits in the East Qinling-Dabie orogenic belt: Characteristics and tectonic settings. *Ore Geol. Rev.* **2011**, *43*, 264–293. [[CrossRef](#)]
21. Zhang, G.W.; Meng, Q.R.; Yu, Z.P.; Sun, Y.; Zhou, D.W.; Guo, A.L. Orogenic process and its dynamic characteristics of the Qinling Orogenic belt. *Sci. Sin. (Terrae)* **1996**, *3*, 193–200.
22. Zhang, Z.W.; Yang, H.Z.; Zhu, B.Q. The Development of Sedimentary Buildups and Mineralization in the Eastern Qinling Mountain. *Acta Geosci. Sin.* **2003**, *24*, 293–298.
23. Li, N.; Ulrich, T.; Chen, Y.-J.; Thomsen, T.B.; Pease, V.; Pirajno, F. Fluid evolution of the Yuchiling porphyry Mo deposit, East Qinling, China. *Ore Geol. Rev.* **2012**, *48*, 442–459. [[CrossRef](#)]
24. Yang, Y.F.; Li, N.; Yang, Y. Fluid inclusion study of the Nannihu porphyry Mo-W deposit, Luanchuan county, Henan province. *Acta Petrol. Sin.* **2009**, *25*, 2550–2562.
25. Xiang, J.; Pei, R.; Ye, H.; Wang, C.; Tian, Z. Source and evolution of the ore-forming fluid in the Nannihu-Sandaozhuang Mo (W) deposit: Constraints from C-H-O stable isotope data. *Geol. China* **2012**, *39*, 1778–1789.
26. Hu, Z.; Gao, S.; Liu, Y.; Hu, S.; Chen, H.; Yuan, H. Signal enhancement in laser ablation ICP-MS by addition of nitrogen in the central channel gas. *J. Anal. Atom. Spectrom.* **2008**, *23*, 1093–1101. [[CrossRef](#)]
27. Hu, Z.; Liu, Y.; Gao, S.; Liu, W.; Zhang, W.; Tong, X.; Lin, L.; Zong, K.; Li, M.; Chen, H.; et al. Improved in situ Hf isotope ratio analysis of zircon using newly designed X skimmer cone and jet sample cone in combination with the addition of nitrogen by laser ablation multiple collector ICP-MS. *J. Anal. Atom. Spectrom.* **2012**, *27*, 1391–1399. [[CrossRef](#)]
28. Liu, Y.; Hu, Z.; Gao, S.; Günther, D.; Xu, J.; Gao, C.; Chen, H. In situ analysis of major and trace elements of anhydrous minerals by LA-ICP-MS without applying an internal standard. *Chem. Geol.* **2008**, *257*, 34–43. [[CrossRef](#)]
29. Liu, Y.; Hu, Z.; Zong, K.; Gao, C.; Gao, S.; Xu, J.; Chen, H. Reappraisal and refinement of zircon U-Pb isotope and trace element analyses by LA-ICP-MS. *Chin. Sci. Bull.* **2010**, *55*, 1535–1546. [[CrossRef](#)]
30. Rudnick, R.; Gao, S. Composition of the Continental Crust. *Ref. Mod. Earth Syst. Environ. Sci.* **2014**, *4*, 1–51.
31. Sun, S.S.; McDonough, W.F. Chemical and isotopic systematics of oceanic basalts: Implications for mantle composition and processes. *Geol. Soc. Lond. Spec. Publ.* **1989**, *42*, 313–345. [[CrossRef](#)]
32. Lin, S. Discussion on mineral chemistry, genesis and evolution of Magnetite. *Acta Mineral. Sin.* **1982**, *3*, 166–174.
33. Dupuis, C.; Beaudoin, G. Discriminant diagrams for iron oxide trace element fingerprinting of mineral deposit types. *Miner. Depos.* **2011**, *46*, 319–335. [[CrossRef](#)]
34. Huang, X.W.; Beaudoin, G. Textures and Chemical Compositions of Magnetite from Iron Oxide Copper-Gold (IOCG) and Kiruna-Type Iron Oxide-Apatite (IOA) Deposits and Their Implications for Ore Genesis and Magnetite Classification Schemes. *Econ. Geol.* **2019**, *114*, 953–979. [[CrossRef](#)]

35. Huang, X.W.; Boutroy, É.; Makvandi, S.; Beaudoin, G.; Corriveau, L.; De Toni, A.F. Trace element composition of iron oxides from IOCG and IOA deposits: Relationship to hydrothermal alteration and deposit subtypes. *Miner. Depos.* **2018**, *54*, 525–552. [[CrossRef](#)]
36. Huang, X.W.; Sappin, A.-A.; Boutroy, É.; Beaudoin, G.; Makvandi, S. Trace Element Composition of Igneous and Hydrothermal Magnetite from Porphyry Deposits: Relationship to Deposit Subtypes and Magmatic Affinity. *Econ. Geol.* **2019**, *114*, 917–952. [[CrossRef](#)]
37. James, B.R. Chromium. In *Encyclopedia of Water Science*; Stewart, B.A., Howell, T.A., Eds.; Marcel Dekker: New York, NY, USA, 2003; pp. 77–82.
38. Nadoll, P.; Mauk, J.L.; Leveille, R.A.; Koenig, A.E. Geochemistry of magnetite from porphyry Cu and skarn deposits in the southwestern United States. *Miner. Depos.* **2015**, *50*, 493–515. [[CrossRef](#)]
39. Toplis, M.J.; Corgne, A. An experimental study of element partitioning between magnetite, clinopyroxene and iron-bearing silicate liquids with particular emphasis on vanadium. *Contrib. Mineral. Petrol.* **2002**, *144*, 22–37. [[CrossRef](#)]
40. Acosta-Gongora, P.; Gleeson, S.A.; Samson, I.M. Trace Element Geochemistry of Magnetite and Its Relationship to Cu-Bi-Co-Au-Ag-U-W Mineralization in the Great Bear Magmatic Zone, NWT, Canada. *Econ. Geol.* **2014**, *109*, 1901–1928. [[CrossRef](#)]
41. Broughm, S.G.; Hanchar, J.M.; Tornos, F.; Westhues, A.; Attersley, S. Mineral chemistry of magnetite from magnetite-apatite mineralization and their host rocks: Examples from Kiruna, Sweden, and El Laco, Chile. *Miner. Depos.* **2017**, *52*, 1223–1244. [[CrossRef](#)]
42. Kotaš, J.; Stasicka, Z. Chromium occurrence in the environment and methods of its speciation. *Environ. Pollut.* **2004**, *107*, 263–283. [[CrossRef](#)]
43. Righter, K.; Leeman, W.P.; Hervig, R.L. Partitioning of Ni, Co and V between spinel-structured oxides and silicate melts: Importance of spinel composition. *Chem. Geol.* **2006**, *227*, 1–25. [[CrossRef](#)]
44. Balan, E.; Villiers, J.P.R.D.; Eeckhout, S.G.; Glatzel, P.; Toplis, M.J.; Fritsch, E.; Allard, T.; Galoisy, L.; Calas, G. The oxidation state of vanadium in titanomagnetite from layered basic intrusions. *Am. Mineral.* **2006**, *91*, 953–956. [[CrossRef](#)]
45. Sun, X.; Lin, H.; Fu, Y.; Li, D.; Hollings, P.; Yang, T.; Liu, Z. Trace element geochemistry of magnetite from the giant Beiya gold-polymetallic deposit in Yunnan Province, Southwest China and its implications for the ore forming processes. *Ore Geol. Rev.* **2017**, *91*, 477–490. [[CrossRef](#)]
46. Zhao, L.; Chen, H.; Zhang, L.; Li, D.; Zhang, W.; Wang, C.; Yang, J.; Yan, X. Magnetite geochemistry of the Heijianshan Fe-Cu (-Au) deposit in Eastern Tianshan: Metallogenic implications for submarine volcanic-hosted Fe-Cu deposits in NW China. *Ore Geol. Rev.* **2018**, *100*, 422–440. [[CrossRef](#)]
47. Fu, Y.; Sun, X.; Li, D.; Lin, H. U-Pb Geochronology and Geochemistry of U-Rich Garnet from the Giant Beiya Gold-Polymetallic Deposit in SW China: Constraints on Skarn Mineralization Process. *Minerals* **2018**, *8*, 128. [[CrossRef](#)]
48. Buddington, A.F.; Lindsley, D.H. Iron-Titanium Oxide Minerals and Synthetic Equivalents. *J. Petrol.* **1964**, *5*, 310–357. [[CrossRef](#)]
49. McIntire, W.L. Trace element partition coefficients—A review of theory and applications to geology. *Geochim. Cosmochim. Acta* **1963**, *27*, 1209–1264. [[CrossRef](#)]
50. Knipping, J.L.; Bilenker, L.D.; Simon, A.C.; Reich, M.; Barra, F.; Deditius, A.P.; Wälle, M.; Heinrich, C.A.; Holtz, F.; Munizaga, R. Trace elements in magnetite from massive iron oxide-apatite deposits indicate a combined formation by igneous and magmatic-hydrothermal processes. *Geochim. Cosmochim. Acta* **2015**, *171*, 15–38. [[CrossRef](#)]
51. O’Neil, H.S.C.; Navrotsky, A. Cation distributions and thermodynamic properties of binary spinel solid solutions. *Am. Mineral.* **1984**, *69*, 733–753.
52. Shannon, R.D.J. Revised Effective Ionic Radii and Systematic Study of Inter Atomic Distances in Halides and Chalcogenides. *Acta Crystallogr. A* **1976**, *32*, 751–767. [[CrossRef](#)]
53. Bau, M. Rare-earth element mobility during hydrothermal and metamorphic fluid-rock interaction and the significance of the oxidation state of europium. *Chem. Geol.* **1991**, *93*, 219–230. [[CrossRef](#)]
54. Bau, M.; Dulski, P. Anthropogenic origin of positive gadolinium anomalies in river waters. *Earth Planet. Sci. Lett.* **1996**, *143*, 245–255. [[CrossRef](#)]
55. Bao, Z.W.; Zeng, Q.S.; Zhao, T.P.; Yuan, Z.L. Geochemistry and petrogenesis of the ore-related Nannihu and Shangfanggou granite porphyries from east Qinling belt and their constraints on the molybdenum mineralization. *Acta Petrol. Sin.* **2009**, *25*, 2523–2536.
56. Flynn, R.T.; Wayne Burnham, C. An experimental determination of rare earth partition coefficients between a chloride containing vapor phase and silicate melts. *Geochim. Cosmochim. Acta* **1978**, *42*, 685–701. [[CrossRef](#)]
57. Ayers, J.C.; Egglar, D.H. Partitioning of elements between silicate melt and H₂O-NaCl fluids at 1.5 and 2.0 GPa pressure: Implications for mantle metasomatism. *Geochim. Cosmochim. Acta* **1995**, *59*, 4237–4246. [[CrossRef](#)]
58. Bai, T.B.; Van Groos, A.K. The distribution of Na, K, Rb, Sr, Al, Ge, Cu, W, Mo, La, and Ce between granitic melts and coexisting aqueous fluids. *Geochim. Cosmochim. Acta* **1999**, *63*, 1117–1131. [[CrossRef](#)]
59. Ghaderi, M.; Palin, J.M.; Campbell, I.H.; Sylvester, P.J. Rare earth element systematics in scheelite from hydrothermal gold deposits in the Kalgoorlie-Norseman region, Western Australia. *Econ. Geol.* **1999**, *94*, 423–437. [[CrossRef](#)]
60. Wood, S.A.; Samson, I.M. The Hydrothermal Geochemistry of Tungsten in Granitoid Environments: I. Relative Solubilities of Ferberite and Scheelite as a Function of T, P, pH, and mNaCl. *Econ. Geol.* **2000**, *95*, 143–182. [[CrossRef](#)]
61. Reed, M.J.; Candela, P.A.; Piccoli, P.M. The distribution of rare earth elements between monzogranitic melt and the aqueous volatile phase in experimental investigations at 800 °C and 200 MPa. *Contrib. Mineral. Petrol.* **2000**, *140*, 251–262. [[CrossRef](#)]

62. Gaspar, M.; Knaack, C.; Meinert, L.D.; Moretti, R. REE in skarn systems: A LA-ICP-MS study of garnets from the Crown Jewel gold deposit. *Geochim. Cosmochim. Acta* **2008**, *72*, 185–205. [[CrossRef](#)]
63. Zhang, Y.; Liu, Q.; Shao, Y.; Li, H. Fingerprinting the Hydrothermal Fluid Characteristics from LA-ICP-MS Trace Element Geochemistry of Garnet in the Yongping Cu Deposit, SE China. *Minerals* **2017**, *7*, 199. [[CrossRef](#)]
64. Allen, D.E.; Seyfried, W.E. REE controls in ultramafic hosted MOR hydrothermal systems: An experimental study at elevated temperature and pressure. *Geochim. Cosmochim. Acta* **2005**, *69*, 675–683. [[CrossRef](#)]
65. Zhai, D.-G.; Liu, J.-J.; Zhang, H.-Y.; Wang, J.-P.; Su, L.; Yang, X.-A.; Wu, S.-H. Origin of oscillatory zoned garnets from the Xieertala Fe-Zn skarn deposit, northern China: In situ LA-ICP-MS evidence. *Lithos* **2014**, *190–191*, 279–291. [[CrossRef](#)]
66. Lu, Y.; Liu, J.; Zhang, D.; Carranza, E.J.M.; Zhai, D.; Ge, L.; Sun, H.; Wang, B.; Chen, Y.; Liu, P. Genesis of the Saishitang skarn type copper deposit, West Qinling, Qinghai Province: Evidence from fluid inclusions and stable isotopes. *Ore Geol. Rev.* **2016**, *75*, 268–283. [[CrossRef](#)]

Disclaimer/Publisher’s Note: The statements, opinions and data contained in all publications are solely those of the individual author(s) and contributor(s) and not of MDPI and/or the editor(s). MDPI and/or the editor(s) disclaim responsibility for any injury to people or property resulting from any ideas, methods, instructions or products referred to in the content.